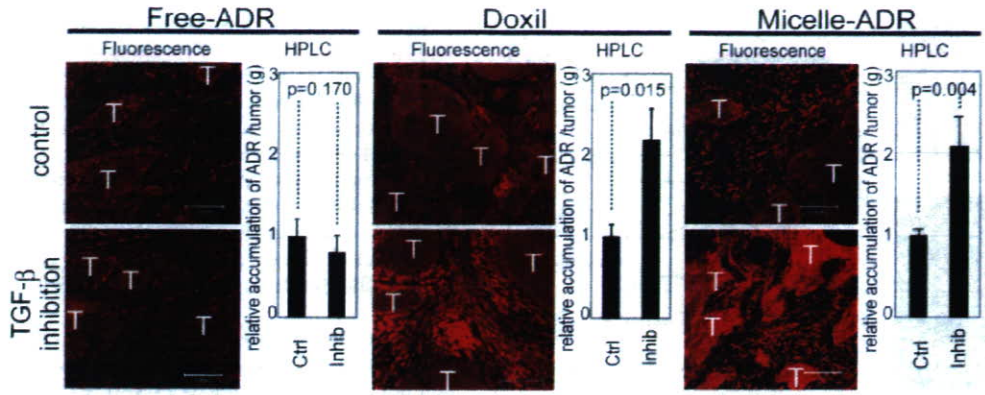

Fig. 3. Biodistribution of ADR in the BxPC3 model. The biodistribution of ADR was investigated in the BxPC3 model by fluorescence examination (T indicates nests of tumor cells in tumor tissues) and by HPLC. The distributions of Doxil, micelle ADR, and free ADR at 8 mg/kg with and without TβR-I inhibitor at 1 mg/kg were examined 24 h after administration. Enhancement of drug accumulation in tumor was specifically observed with TβR-I inhibitor with Doxil and micelle ADR. Error bars in the graphs represent standard errors, and *P* values were calculated by Student's *t* test. Ctrl, control; Inhib, inhibitor.

from that in the control (SI Fig. 12). On the other hand, low-dose TβR-I inhibitor specifically suppressed the phosphorylation of Smad2 in vascular endothelium (SI Fig. 11*B*). These findings suggest that the use of small-molecule TβR-I inhibitor at low doses is advantageous for limiting adverse effects.

We thus hypothesized that low-dose TβR-I inhibitor may enhance the accumulation of nanocarriers, the molecular sizes of which are similar to 2-MDa dextran, in hypovascular solid tumors. We used two nanocarriers to test this hypothesis: Doxil (26), a liposomal ADR, and a core–shell type polymeric micelle-encapsulating ADR (micelle ADR) that we developed (22). The latter is a micellar nanocarrier consisted of block copolymers in which ADR is conjugated to the PEG chain through an acid–labile linkage. This drug carrier releases free ADR molecules selectively in acidic conditions, e.g., in intracellular endosomes and lysosomes (SI Fig. 7). We tested the effects of i.p. administration of TβR-I inhibitor with i.v. administration of Doxil or micelle ADR at 8 mg/kg on size-matched xenografts of BxPC3 cells, which are ADR-sensitive *in vitro* (12). Conventional ADR without drug carriers (free ADR), a small-molecule compound of MW 543.52, was also used for comparison. We first examined the distribution of ADR molecules in tumor tissues by using confocal imaging of fluorescence of ADR and HPLC (Fig. 3). The fluorescence of ADR molecules in micelle ADR is detectable only when ADR molecules are released from the micelle, whereas that in Doxil is detectable even when it is encapsulated in the liposome. The total amount of accumulated ADR, the sum of that in cancer cells and the cancer microenvironment, is measured by HPLC, which detects ADR molecules with and without drug carriers. Administration of TβR-I inhibitor with the nanocarriers yielded significant enhancement of intratumoral accumulation of ADR molecules. Because TβR-I inhibitor did not increase the accumulation of free ADR, we suspected that only macromolecules would be benefited by the use of TβR-I inhibitor through enhancement of EPR effect.

We then examined the growth-inhibitory effects of these anticancer drugs with and without TβR-I inhibitor on size-matched BxPC3 xenografts. As shown in Fig. 4*A*, the growth curves of the BxPC3 xenografts confirmed the findings for the distribution of ADR molecules. None of free ADR, Doxil, micelle ADR as monotherapy, or free ADR with TβR-I inhibitor significantly reduced tumor growth. In contrast, ADR encapsulated in nanocarriers exhibited significant effects on the growth of tumor when combined with TβR-I inhibitor (see *SI List* for statistical study).

Because micelle ADR was more effective than Doxil (as shown in Figs. 3 and 4*A*), and the maximum tolerated dose of micelle ADR is far higher than one shot of 8 mg/kg (22, 26) (the dose in Fig. 4*A*), we further tested the growth-inhibitory effects of an increased dose of micelle ADR combined with TβR-I inhibitor (Fig. 4*B*). When micelle ADR or free ADR was

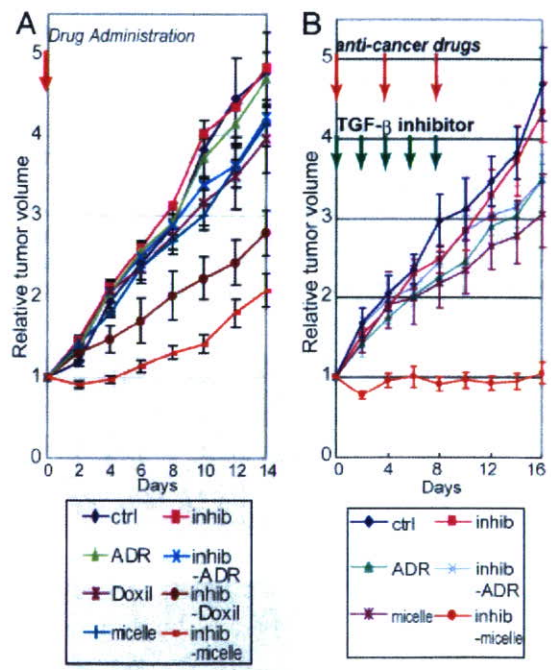

Fig. 4. Effects of TβR-I inhibitor on anti-tumor activity of nanocarriers, incorporating ADR in the BxPC3 model. (*A*) Free ADR, liposomal ADR (Doxil), micelle ADR (micelle) or vehicle control (ctrl) was administered i.v. in a single bolus with and without TβR-I inhibitor (inhib) i.p. to xenografted mice in which tumors had been allowed to grow for a few weeks before treatment ($n = 5$). Relative tumor sizes were measured every second day and are shown as a growth curve with bars showing standard errors. Only nanocarriers administered together with TβR-I inhibitor exhibited significant reduction of growth compared with the control. (*B*) Growth curve study with an increased dose of micelle ADR. With the day of initiation of drug administration designated day 0, anticancer drugs were administered i.v. on days 0, 4, and 8 with and without i.p. TβR-I inhibitor on days 0, 2, 4, 6, and 8. Further growth-inhibitory effect was observed with an increase in dose of micelle ADR. (Results of multivariate ANOVA study are shown in *SI List*.)

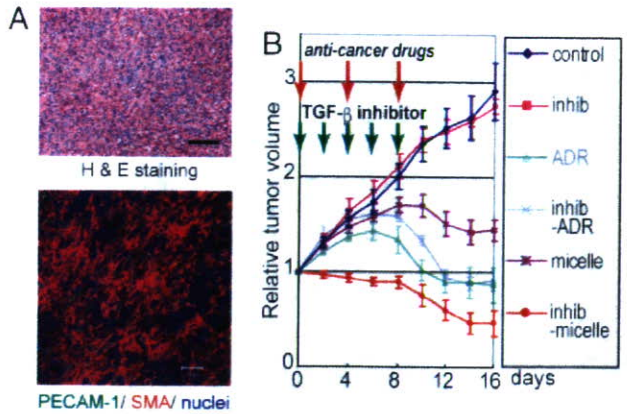

Fig. 5. Growth-curve study in the MiaPaCa-2 pancreatic cancer xenograft model. (*A*) TGF-β-nonresponsive MiaPaCa-2 cell xenografts exhibited an undifferentiated pattern of histology on H&E staining (*Upper*), with rich SMA-positive fibrotic tissue (show in red in *Lower*) and much less PECAM-1-positive vasculature (shown in green) compared with the BxPC3 model. (*B*) The same experimental protocol as in Fig. 4*B* was used in the model, and the effectiveness of the use of TβR-I inhibitor was confirmed. Inhib, inhibitor; micelle, micelle-ADR. (Results of multivariate ANOVA for the growth-curve studies are shown in *SI List*.)

administered on days 0, 4, and 8, with and without TβR-I inhibitor, only micelle ADR administered together with TβR-I inhibitor exhibited nearly complete growth-inhibitory effect on the tumor in this model. We therefore used this regimen in the following experiments.

The efficacy of combined treatment was further confirmed by using micelle ADR in two other animal models of pancreatic adenocarcinoma. We used size-matched xenograft models of MiaPaCa-2 and Panc-1 cell lines, which are both ADR-sensitive *in vitro* (12) (Fig. 5 and SI Figs. 13 and 14). MiaPaCa-2 is nonresponsive to TGF-β signaling because of TβR-II deficiency, whereas Panc-1 has no deficiency in TGF-β signaling components and responds to TGF-β. On histological examination, the xenografts of MiaPaCa-2 and Panc-1 exhibited similar undifferentiated pattern with scattered cancer cells, rich fibrous tissue, and sparse vasculature distributed homogeneously, unlike that of BxPC3 xenografts (Fig. 5*A* and SI Fig. 14*A*). Use of low-dose TβR-I inhibitor in these models again significantly enhanced the growth-inhibitory effects of micelle ADR (see Fig. 5*B*, SI Fig. 14*B*, and *SI List* for statistical analyses). Effects of free ADR were again not enhanced by TβR-I inhibitor, although the drug itself exhibited some degree of growth-inhibitory effect on the MiaPaCa-2 xenografts. Analysis of the biodistribution of ADR molecules (SI Figs. 13 and 14 *C* and *D*) confirmed the effects of TβR-I inhibitor on accumulation of micelle ADR in these cancer models.

We also tested the growth-inhibitory effect of TβR-I inhibitor and micelle ADR in an orthotopic model of the OCUM-2MLN cell line, which responds to TGF-β (27) (Fig. 6). OCUM-2MLN was derived from a patient with another intractable solid tumor, diffuse-type gastric cancer. The cancer cells were implanted in the gastric wall of nude mice and allowed to grow *in situ* for 2 weeks, leading to formation of hypovascular and fibrotic tumors in the gastric wall (Fig. 6*A*). Tumor area (framed by arrowheads in Fig. 6*B*, *Left*) was measured before the initiation of drug administration, and tumor growth was evaluated by calculating the relative tumor area at day 16 by measuring tumor area again (Fig. 6*B*, *Right*). Significant reduction of tumor growth was again observed only in the mice treated with TβR-I inhibitor and micelle ADR. The distribution of ADR, as detected by fluorescence, confirmed this growth-inhibitory effect (data not shown). These findings suggest that the use of TβR-I inhibitor may enhance the accumulation of nanocarriers in hypovascular solid tumors.

Finally, we examined whether low-dose TβR-I inhibitor increases EPR effect specifically in tumor tissues and not in normal organs. Although nanocarriers were originally designed to decrease the drug accumulation in normal organs, it is important to determine whether use of TβR-I inhibitor exacerbates their side effects (SI Fig. 15). In liver, spleen, kidney, blood, and heart, accumulation of ADR as determined by HPLC was not significantly increased by TβR-I inhibitor (SI Fig. 15 *A* and *B*). Neither dermatitis nor phlebitis around the tail veins was exacerbated by addition of TβR-I inhibitor (SI Fig. 15*C*). In addition, the weight

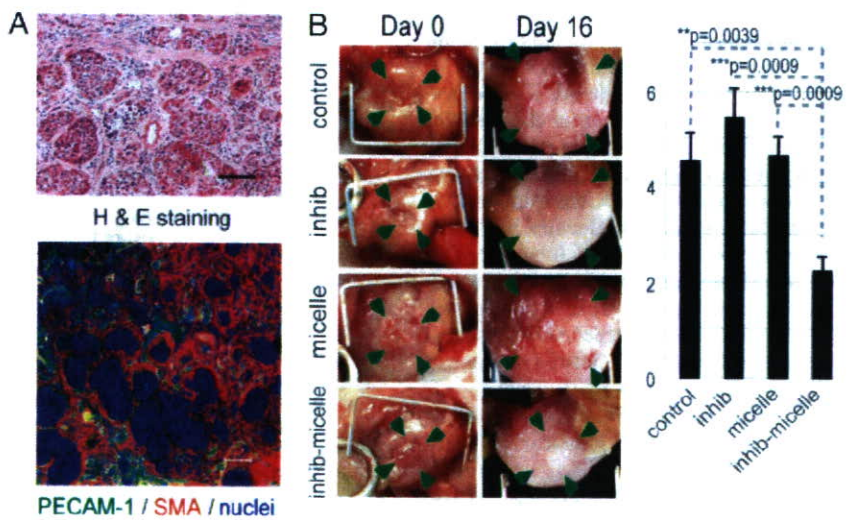

Fig. 6. Effects of TβR-I inhibitor administered together with micelle ADR in an orthotopic diffuse-type gastric cancer model. OCUM-2MLN, a human diffuse-type gastric cancer cell line, was inoculated into the gastric wall of nude mice ($n = 5$). Two weeks after inoculation, the cancer tissues exhibited diffuse-type histology on H&E staining (*A Upper*) with sparse formation of blood vessels (PECAM-1 staining, shown in green) (*A Lower*). The sizes of tumors on the gastric wall were measured based on tumor areas (*B Left*), and the values on day 16 were divided by those on day 0, the day of initiation of drug administration, to obtain relative tumor areas. Relative tumor areas are shown with bars for standard errors (*B Right*). TβR-I inhibitor significantly reduced tumor growth in this model, as well. *P* values were calculated by Student's *t* test. Inhib, inhibitor; micelle, micelle-ADR.

of mice that were treated with micelle ADR was not significantly affected by TβR-I inhibitor (data not shown). These findings in normal organs strongly suggest that low-dose TβR-I inhibitor enhances EPR effect only in tumors and that exacerbation of toxicity or side effects of nanocarrier-encapsulated drugs may be minimal with this treatment.

Discussion

In the present study, we have tested a use of TβR-I inhibitor at a low dose to induce alteration in cancer-associated neovasculature to exhibit more leakiness for macromolecules, with less pericyte-coverage and greater endothelial area (Figs. 1 and 2). Because use of TβR-I inhibitor induced the same alteration in neovasculature in the Matrigel plug assay (M.R.K., unpublished data), a model of adult neoangiogenesis (23), the effects of use of TβR-I inhibitor on tumor vasculature observed in the present study may be common in adult neoangiogenesis. Although the roles of growth factors, including TGF-β, may differ during development and in adults, these phenotypes are reminiscent of those of knockout mice deficient in certain components of TGF-β signaling, e.g., endoglin (28, 29), ALK-1 (30, 31), and ALK-5 (32), in which loss of pericyte-coverage and dilatation of the vasculature in yolk sac or embryos were observed. These phenotypes are also consistent with the findings obtained on *in vitro* culture of endothelial cell lineages (33) and mesenchymal progenitor cells (34), which showed that pericyte maturation is promoted, and endothelial proliferation is inhibited, by TGF-β signaling. Vascular phenotypes due to defects in TGF-β signaling *in vivo* are also observed in two types of hereditary hemorrhagic telangiectasia (35, 36), which are induced by deficiencies of endoglin or ALK-1, which are components of TGF-β signaling in vascular endothelium. Because of inborn and life-long abnormality of TGF-β signaling in vasculature, these diseases result in a tendency toward hemorrhage in capillaries that is due to vulnerability of the vascular structure. These observations suggest that use of TβR-I inhibitor at a dose corresponding to that in mice in our study may have similar effects in humans. However, the inhibition of TGF-β signaling is only transient in our method, because of the use of small-molecule inhibitor, and the effects of TβR-I inhibitor may thus be far less severe than the phenotypes observed in hereditary hemorrhagic telangiectasia.

The changes in tumor neovasculature induced by TβR-I inhibitor resulted in enhanced extravasation of molecules, although in a molecular-size dependent manner. Accumulation of 2-MDa dextran with a 50-nm hydrodynamic diameter, Doxil with a 108-nm diameter, and micelle ADR with a 65-nm diameter was enhanced by TβR-I inhibitor in the present study, although accumulation of small-molecule agents, including ADR (MW 543.52) and BrdU (MW 307.10) (M.R.K., unpublished data), was not significantly enhanced. Dreher *et al.* (24) recently reported the molecular-size-dependency of intratumoral drug distribution, using a xenograft model of FaDu cells derived from human hypopharyngeal squamous cell carcinoma. They used several dextrans with molecular sizes ranging from 3.3 kDa to 2 MDa, with estimated hydrodynamic diameters of 3.5 nm to 50 nm, respectively. Dextran molecules of 3.3 kDa and 10 kDa, the smallest ones tested, were found to penetrate deeply and homogeneously into tumor tissue, although they remained in tumor tissue only transiently, for far less than 30 min. However, larger dextran of 2 MDa with a diameter of 50 nm, which we also used in the present study, for the most part remained in the vasculature in cancer tissue and reached only an ≈5-μm distance from the vessel wall at 30 min after injection. Although the histological characteristics of their model, which were not described in their report, may differ from those of the cancer models used in our study, the distribution of 2-MDa dextran observed by Dreher *et al.* agrees with that obtained without TβR-I inhibitor in the BxPC3 xenografts observed in the present study (Fig. 3). TβR-I inhibitor could thus enhance the accumulation of macromolecules with hydrodynamic diameters of >50 nm, common sizes for nanocarriers, in cancers other than those used in the present study. However, the range of sizes of macromolecules and histological patterns of cancer for which use of TβR-I inhibitor can exhibit enhancing effects remains to be determined.

In conclusion, we have proposed here a use of small-molecule TβR-I inhibitor at a low dose to enhance EPR effect in intractable solid cancers. This method could be a breakthrough in chemotherapy by using nanocarriers in these cancers. Because low-dose TβR-I inhibitor does not affect cancer cells, it may reduce the potential side effects of TGF-β inhibitors, and its enhancing effect is independent of the reactivity of cancer cells to TGF-β signaling. Use of TGF-β inhibitors may thus enable reduction of the systemic doses of nanocarriers and thereby decrease the adverse effects of anticancer drugs.

Methods

TGF-β Inhibitors, Anticancer Drugs, and Antibodies. TβR-I inhibitor was purchased from Calbiochem (San Diego, CA) (LY364947; catalog no. 616451). ADR was obtained from Nippon Kayaku (Tokyo, Japan) and purchased from Kyowa Hakko (Tokyo, Japan). Doxil was purchased from Alza (Mountain View, CA). Micelle ADR was prepared as reported (22) (see *SI Materials and Methods* for detailed information). The antibodies to PECAM-1 and VE-cadherin were from BD PharMingen (San Diego, CA), those to neuroglycan 2 and collagen IV were from Chemicon (Temecula, CA), and that to SMA was from Sigma–Aldrich (St. Louis, MO). The anti-phospho-Smad2 antibody was a gift from A. Moustakas and C.-H. Heldin (Ludwig Institute for Cancer Research, Uppsala, Sweden).

Cancer Cell Lines and Animals. BxPC3, MiaPaCa-2, and Panc-1 human pancreatic adenocarcinoma cell lines were obtained from the American Type Culture Collection (Manassas, VA). The OCUM-2MLN human diffuse-type gastric cancer cell line was previously established (27). BxPC3 cells were grown in RPMI medium 1640 supplemented with 10% FBS. MiaPaCa-2, Panc-1, and OCUM-2MLN cells were grown in DMEM with 10% FBS. BALB/c nude mice, 5–6 weeks of age, were obtained from CLEA Japan (Tokyo, Japan), Sankyo Laboratory (Tokyo, Japan), and Charles River Laboratories, (Tokyo, Japan). All animal experimental protocols were performed in accordance with the policies of the Animal Ethics Committee of the University of Tokyo.

Cancer Models. The effects of anticancer drugs were assessed by s.c. implantation of cancer cells into nude mice, and by orthotopic inoculation of OCUM-2MLN cells into the gastric walls of nude mice. A total of 5×10^6 cells in 100 μl of PBS for the xenograft models and the same number in 50 μl of PBS for the orthotopic model were injected into male nude mice and allowed to grow for 2–3 weeks to reach proliferative phase, before initiation of drug administration. For growth-curve studies, the day of initiation of drug administration was considered day 0, and TβR-I inhibitor, dissolved to 5 mg/ml in DMSO and diluted by 100 μl of PBS, or the vehicle control, was injected i.p. at 1 mg/kg on day 0 only in the experiment shown in Fig. 4*A* and on days 0, 2, 4, 6, and 8 in other experiments. Doxil, micelle ADR, and free ADR at 8 mg/kg, or normal saline as vehicle control, were also administered i.v. in 200 μl/vol via the tail vein on day 0 (Fig. 4*A*). In other experiments, micelle ADR at 16 mg/kg, free ADR at 8 mg/kg, or normal saline was also administered i.v. on days 0, 4, and 8. There were five mice per group per cell line. The doses of ADR and Doxil were determined based on the lethal doses in mice (22, 26). For biodistribution studies, three mice per group per cell line were treated with 8 mg/kg Doxil, micelle

ADR, or free ADR i.v., with and without TβR-I inhibitor at 1 mg/kg i.p. The mice were examined 24 h after injection.

Quantification in Tumor Models. Xenograft tumors were measured externally every second day until day 16, and tumor volume was approximated by using the equation vol = $(a \times b^2)/2$, where vol is volume, a the length of the major axis, and b is the length of the minor axis. Relative tumor volume was calculated by dividing tumor volume by that on day 0 (the day of initiation of treatment), where actual estimated volumes of xenografted tumors in mm^3 at initiation of drug administration were as follows (mean ± standard error): BxPC3 (in Fig. 4*A*), 76.4± 7.0; BxPC3 (in Fig. 4*B*), 74.4 ± 3.3; MiaPaCa-2, 221.2 ± 12.7; and Panc-1, 242.16 ± 24.5. For orthotopic OCUM-2MLN tumors, the area of the primary focus on the gastric wall was measured in Adobe Photoshop software, by opening the abdomen before initiation of treatment and at the end of the observation period. Relative tumor area was calculated by dividing tumor area by that on the day of initiation of treatment. The results were further analyzed statistically by the multivariate ANOVA test, using JMP6 software (SAS Institute, Raleigh, NC).

Histology and Immunohistochemistry. The excised samples were either directly frozen in dry-iced acetone for immunohistochemistry, or fixed overnight in 4% paraformaldehyde and then paraffin-embedded to prepare them for H&E or AZAN staining. Frozen samples were further sectioned at 10-μm thickness in a cryostat, briefly fixed with 10% formalin, and then incubated with primary and secondary antibodies. TOTO-3 for nuclear staining, Alexa488-, Alexa594-, and Alexa647-conjugated secondary antibodies, anti-rat and rabbit IgGs, Zenon labeling kit anti-rabbit and mouse IgG, and FITC-conjugated dextran (MW 2×10^6) were purchased from Invitrogen Molecular Probes (Eugene, OR). Samples were observed by using a Zeiss (Thornwood, NY) LSM510 Meta confocal microscope for immunohistochemistry, and an Olympus (Tokyo, Japan) AX80 microscope for H&E and AZAN staining.

Biodistribution. Xenografts were inoculated s.c. in nude mice and allowed to grow for 2–3 weeks before drug administration. We then injected TβR-I inhibitor at 1 mg/kg i.p. together with i.v. administration of Doxil, micelle ADR, or free ADR at 8 mg/kg. The tumors or organs were excised 24 h after injection of drugs, and frozen in dry-iced acetone to obtain fluorescence images or weighed and mixed with daunorubicin commensurate with the sample weight as an internal control and then frozen to prepare them for measurement by HPLC. The HPLC method used for analyses is described in ref. 22. To obtain fluorescence images, we performed cryostat sectioning of the frozen samples and washed the sections twice briefly with PBS but did not fix them to avoid elution of ADR. The samples were then observed with a Zeiss confocal microscope, using an excitation laser at 488 nm and a detection filter for the infrared region.

We thank Erik Johansson (University of Tokyo) for assistance. This work was supported by a Kakenhi (Grant-in-Aid for Scientific Research) in Priority Areas "New strategies for cancer therapy based on advancement of basic research" and the Project on the Materials Development for Innovative Nano-Drug Delivery Systems from the Ministry of Education, Culture, Sports, Science, and Technology of Japan. This work was also supported by the Foundation for Promotion of Cancer Research in Japan.

1. Muggia FM (2001) *Curr Oncol Rep* 3:156–162.
2. Ferrari M (2005) *Nat Rev Cancer* 5:161–171.
3. Hassan M, Little RF, Vogel A, Aleman K, Wyvill K, Yarchoan R, Gandjbakhche AH (2004) *Technol Cancer Res Treat* 3:451–457.
4. Emoto M, Udo T, Obama H, Eguchi F, Hachisuga T, Kawarabayashi T (1998) *Gynecol Oncol* 70:351–357.
5. Duncan R (2006) *Nat Rev Cancer* 6:688–701.
6. Kataoka K, Harada A, Nagasaki Y (2001) *Adv Drug Deliv Rev* 47:113–131.
7. Hamaguchi T, Matsumura Y, Suzuki M, Shimizu K, Goda R, Nakamura I, Nakatomi I, Yokoyama M, Kataoka K, Kakizoe T (2005) *Br J Cancer* 92:1240–1246.
8. Nishiyama N, Okazaki S, Cabral H, Miyamoto M, Kato Y, Sugiyama Y, Nishio K, Matsumura Y, Kataoka K (2003) *Cancer Res* 63:8977–8983.
9. MacKenzie MJ (2004) *Lancet Oncol* 5:541–549.
10. Fuchs CS, Mayer RJ (1995) *N Engl J Med* 333:32–41.
11. Burris HA, III, Moore MJ, Andersen J, Green MR, Rothenberg ML, Modiano MR, Cripps MC, Portenoy RK, Storniolo AM, Tarassoff P, *et al.* (1997) *J Clin Oncol* 15:2403–2413.
12. Watanabe N, Tsuji N, Tsuji Y, Sasaki H, Okamoto T, Akiyama S, Kobayashi D, Sato T, Yamauchi N, Niitsu Y (1996) *Pancreas* 13:395–400.
13. Matsumura Y, Maeda H (1986) *Cancer Res* 46:6387–6392.
14. Maeda H, Matsumura Y (1989) *Crit Rev Ther Drug Carrier Syst* 6:193–210.
15. Sofuni A, Iijima H, Moriyasu F, Nakayama D, Shimizu M, Nakamura K, Itokawa F, Itoi T (2005) *J Gastroenterol* 40:518–525.
16. Takahashi Y, Cleary KR, Mai M, Kitadai Y, Bucana CD, Ellis LM (1996) *Clin Cancer Res* 2:1679–1684.
17. Roberts AB, Wakefield LM (2003) *Proc Natl Acad Sci USA* 100:8621–8623.
18. Feng XH, Derynck R (2005) *Annu Rev Cell Dev Biol* 21:659–693.
19. Bandyopadhyay A, Agyin JK, Wang L, Tang Y, Lei X, Story BM, Cornell JE, Pollock BH, Mundy GR, Sun L-Z (2006) *Cancer Res* 66:6714–6721.
20. Yingling JM, Blanchard KL, Sawyer JS (2004) *Nat Rev Drug Discov* 3:1011–1022.
21. Sawyer JS, Anderson BD, Beight DW, Campbell RM, Jones ML, Herron DK, Lampe JW, McCowan JR, McMillen WT, Mort N, *et al.* (2003) *J Med Chem* 46:3953–3956.
22. Bae Y, Nishiyama N, Fukushima S, Koyama H, Matsumura Y, Kataoka K (2005) *Bioconjug Chem* 16:122–130.
23. Kano MR, Morishita Y, Iwata C, Iwasaka S, Watabe T, Ouchi Y, Miyazono K, Miyazawa K (2005) *J Cell Sci* 118:3759–3768.
24. Dreher MR, Liu W, Michelich CR, Dewhirst MW, Yuan F, Chilkoti A (2006) *J Natl Cancer Inst* 98:335–344.
25. McDonald DM, Choyke PL (2003) *Nat Med* 9:713–725.
26. Gabizon A, Tzemach D, Mak L, Bronstein M, Horowitz AT (2002) *J Drug Target* 10:539–548.
27. Yashiro M, Chung YS, Nishimura S, Inoue T, Sowa M (1996) *Clin Exp Metastasis* 14:43–54.
28. Li DY, Sorensen LK, Brooke BS, Urness LD, Davis EC, Taylor DG, Boak BB, Wendel DP (1999) *Science* 284:1534–1537.
29. Arthur HM, Ure J, Smith AJ, Renforth G, Wilson DI, Torsney E, Charlton R, Parums DV, Jowett T, Marchuk DA, *et al.* (2000) *Dev Biol* 217:42–53.
30. Oh SP, Seki T, Goss KA, Imamura T, Yi Y, Donahoe PK, Li L, Miyazono K, ten Dijke P, Kim S, *et al.* (2000) *Proc Natl Acad Sci USA* 97:2626–2631.
31. Urness LD, Sorensen LK, Li DY (2000) *Nat Genet* 26:328–331.
32. Larsson J, Goumans MJ, Sjostrand LJ, van Rooijen MA, Ward D, Leveen P, Xu X, ten Dijke P, Mummery CL, Karlsson S (2001) *EMBO J* 20:1663–1673.
33. Watabe T, Nishihara A, Mishima K, Yamashita J, Shimizu K, Miyazawa K, Nishikawa S-I, Miyazono K (2003) *J Cell Biol* 163:1303–1311.
34. Hirschi KK, Rohovsky SA, D'Amore PA (1998) *J Cell Biol* 141:805–814.
35. Lebrin F, Deckers M, Bertolino P, ten Dijke P (2005) *Cardiovasc Res* 65:599–608.
36. Fernandez-L A, Sanz-Rodriguez F, Blanco FJ, Bernabeu C, Botella LM (2006) *Clin Med Res* 4:66–78.

J|A|C|S
COMMUNICATIONS

Published on Web 04/05/2007

A Protein Nanocarrier from Charge-Conversion Polymer in Response to Endosomal pH

Yan Lee,[†] Shigeto Fukushima,[‡] Younsoo Bae,[†,§] Shigehiro Hiki,[‡,||] Takehiko Ishii,[#] and Kazunori Kataoka*[,†,‡,§,||,#]

Division of Clinical Biotechnology, Center for Disease Biology and Integrative Medicine, Graduate School of Medicine, Department of Materials Engineering, Center for NanoBio Integration, CREST, Japan Science and Technology Corporation, and Department of Bioengineering, University of Tokyo, 7-3-1 Hongo, Bunkyo-ku, Tokyo 113-0033, Japan

Received February 14, 2007; E-mail: kataoka@bmw.t.u-tokyo.ac.jp

Smart polymers, whose characteristics change in response to an external signal, such as electric potential, magnetic field, temperature, light, and pH, etc., are spotlighted in various research fields including analytical chemistry, tissue engineering, and drug delivery.[1] Especially, the smart polymers, which are sensitive to biosignals, that is, reductive potential[2] or pH, are very attractive in the drug delivery field requiring selective controlled-release. Some pH-sensitive polymers are even facilitating the endosomal escape of drugs by a membrane interaction and/or an increase in the local osmotic pressure.[3]

pH-Sensitive polymers developed so far that release drugs in the endosomal component use acetal, hydrazone, and orthoester bonds, etc.[4] Although they showed a selective degradation in the endosome, their drug release in response to pH was relatively passive and slow. A more active and prompt response to a small pH drop is needed for more effective drug delivery, for example, the specific release in the early endosome.

Citraconic anhydride is an α-methyl derivative of maleic anhydride, which can be used to mask the charge of proteins. As shown in Scheme 1, amide bonds are formed from the reaction between primary amines and citraconic anhydride. The resulting amides have negative charges owing to the carboxylate groups at the end. The citraconic amide is stable at both neutral and basic pH, but it becomes unstable at acidic pH and promptly degrades back into the cationic primary amine. It has been reported that the citraconic amide degrades around pH 5.[5] Therefore, we considered that the citraconic amide could provide a pH-dependent degradability to the polymers that can be selectively functionalized during the early endosome in a cell. Because the degradation was directly related to the charge-conversion, it could also provide an abrupt change in the interaction with counter-ions.

In this study, we synthesized a block copolymer with combtype side groups of the citraconic amide and characterized their physicochemical properties such as the degree of degradability and the charge conversion. With this polymer, we also developed a novel nanocontainer that can promptly release its protein cargo by generating a repulsive electrostatic force owing to the charge-conversion at the endosomal pH.

The synthesis of the diblock copolymer, poly(ethylene glycol)-poly[(*N*'-citraconyl-2-aminoethyl)aspartamide] (PEG-pAsp(EDA-Cit)) (**4**) is illustrated in Scheme 1. The diblock copolymer **2** was synthesized as previously reported.[6] Briefly, the ring-opening polymerization of β-benzyl-L-aspartate *N*-carboxy-anhydride (BLA-NCA) was initiated by the terminal primary amino group of α-methoxy-ω-amino poly(ethylene glycol) (M_n = 12 000) (**1**), and the reaction produced **2**. The prepared **2** was further modified into PEG-poly[(2-aminoethyl)aspartamide] (**3**) by aminolysis with excess ethylenediamine. Finally, **4** was synthesized from **3** and the citraconic anhydride in the pyridine solvent. The detailed synthetic procedures are described in the Supporting Information.

Scheme 1. Synthesis of PEG-pAsp(EDA-Cit): (a) BLA-NCA/DMF; (b) Ethylenediamine/DMF; (c) Citraconic Anhydride (or Succinic Anhydride)/pyridine

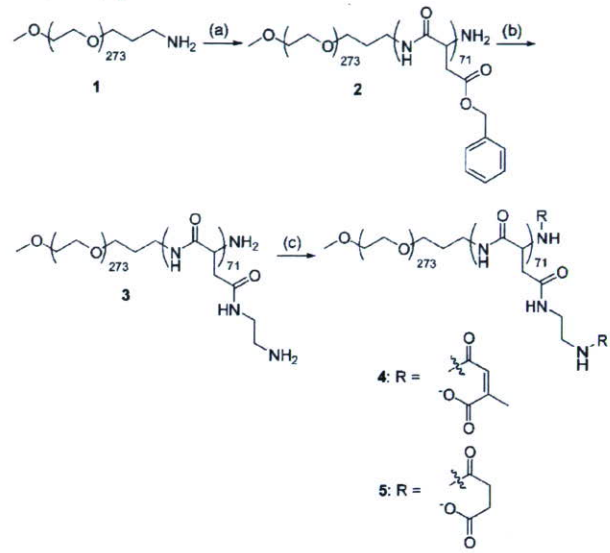

The pH-dependent degradation rates of the citraconic amide of **4** are shown in Figure 1. The degradation rate was calculated by measurement of the primary amine concentration in the polymer at 37 °C. The fluorescamine method was used for the quantification of the amine concentration.[7] In the meantime, PEG-pAsp(EDA-Suc) (**5**) was synthesized as the negative control by mixing **4** with succinic anhydride instead of citraconic anhydride. Although **5** has a structure similar to **4**, **5** does not degrade under acidic pH conditions. The experiments showed that approximately 80% of the citraconic amides was degraded in the acetate buffer (pH 5.5) within 1 h, while 60% of the citraconic amides remained intact in the phosphate buffer (pH 7.4) even after 5 h. No degradation was observed in the case of the succinic amides under both pH conditions.

We previously reported that the formation and characterization of the PIC micelles between the PEG-polyaspartate (PEG-pAsp) and lysozyme, of which the isoelectric point occurs at pH 10.[8]

† Center for Disease Biology and Integrative Medicine, University of Tokyo.
‡ Department of Materials Engineering, University of Tokyo.
§ Center for Nanobio Integration, University of Tokyo.
|| CREST, Japan Science and Technology Corporation.
Department of Bioengineering, University of Tokyo.

10.1021/ja071090b CCC: $37.00

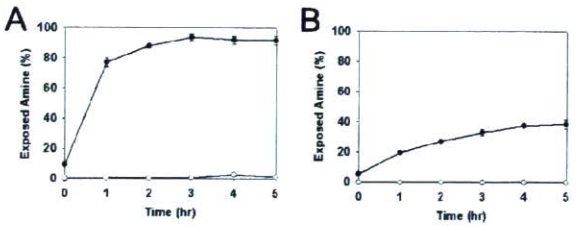

Figure 1. The degradation of citraconic amide (●) and succinic amide (○) in 4 and 5 at pH 5.5 (A) and pH 7.4 (B). The data are expressed as mean values (± standard deviation) of three experiments.

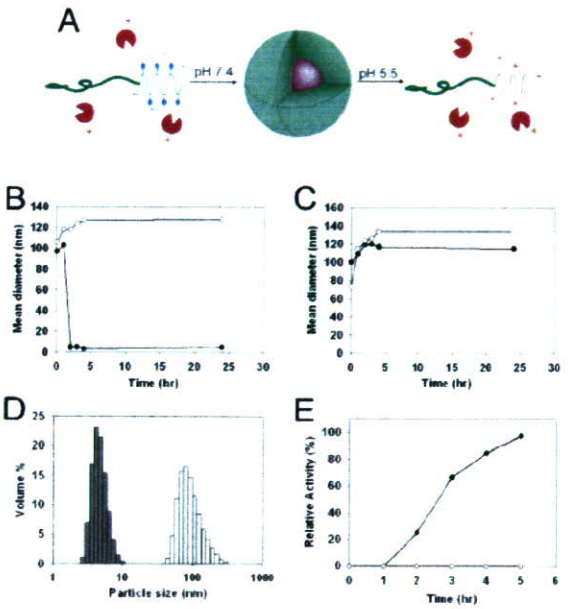

Figure 2. Formation and dissociation of the PIC micelles: (A) schematic diagram for the formation and dissociation of the PIC micelles; the time course of the mean diameter of the PIC micelles of (B) PEG-pAsp(EDA-Cit) and (C) PEG-pAsp(EDA-Suc); (D) the DLS histogram of the PIC micelles at 0 h (white) and at 2 h (gray) at pH 5.5; and (E) the relative lysozyme activity of the PIC micelles. The black dots (●) represent the data at pH 5.5 and the white dots (○) are at pH 7.4.

Following the experimental protocols, the PIC micelles were prepared by mixing **4** and the lysozyme. The pH-dependent stability of the micelles was analyzed by dynamic light scattering (DLS) measurements. The measurements demonstrated that the PIC micelles were successfully formed. More notably, it also suggested that these micelles would be destabilized at the endosomal pH by the degradation of the citraconic amides in **4** accompanied by the charge conversion from negative to positive (Figure 2A).

Figure 2B demonstrates that the size of the micelles prepared from **4** and the lysozymes was stabilized with a diameter of about 130 nm at pH 7.4 even after incubation at 37 °C for 24 h. However, the PIC micelles were promptly dissociated at pH 5.5 within 2 h. The pH dependent profiles of the PIC micelles from **5** and the lysozymes are shown in Figure 2C. As expected, the succinic amide-based micelles were stable at both pH values after 24 h. Figure 2D shows the size distribution of the citraconic amide-based micelles before and after the dissociation. The micelles showed a unimodal size distribution before the dissociation. The distribution around 4.8 nm after a 2-hr incubation resulted from the single lysozyme molecule.[8]

Figure 2E shows the activity of the lysozyme released from the PIC micelles. The lysozyme activity was measured by the well-known method using the *Micrococcus luteus* cell suspension.[9] The relative activity is expressed as a percentage of the free-lysozyme activity. Because the activity depends on the pH, the free-lysozyme activity at each pH was used for the calculation of relative activity.

At pH 7.4, no lysozyme activity was observed for over 5 h. However, at pH 5.5, the PIC micelles showed a lysozyme activity after 2 h, and it increased and reached 97% of the free-lysozyme activity after 5 h. Interestingly, it took 3 h more to observe the full lysozyme activity after the dissociation of the micelles. Considering the fact that the micelles dissociated within 2 h, it is suggested that there is a weak interaction between the lysozyme and block copolymer chains at least 3 h after the dissociation of the micelles. Because the direct contact between lysozyme and the bacterial cell wall is required for the full activity, PEG chain bound to lysozyme, even though the binding is very weak, can reduce the lysozyme activity. After 80% degradation, **4** cannot form the PIC micelles with lysozyme, but it can still repress the lysozyme activity below 5% (data not shown). Nevertheless, it was confirmed that the citraconic amide-based micelles can selectively dissociate and release the lysozyme while maintaining its enzymatic activity by responding to the change in pH.

In summary, we synthesized the charge-converting block copolymer using the citraconic amide as a pH-sensitive charge masking group. The citraconic amide-based block copolymer was selectively degraded in response to the endosomal pH and formed PIC micelles with the cationic model protein, that is, the lysozyme. Most notably, the micelles selectively released the active lysozyme promptly by sensing the change in pH corresponding to the acidic conditions in the intracellular endosomal compartments. Therefore, it was concluded that our stimuli-sensitive block copolymers are promising designs for future drug and gene delivery systems.

Acknowledgment. This work was supported by the Core Research for Evolutional Science and Technology (CREST) from the Japan Science and Technology Agency (JST) as well as by Special Coordination Funds for Promoting Science and Technology from the Ministry of Education, Culture, Sports, Science and Technology of Japan (MEXT).

Supporting Information Available: Materials and methods, the temperature-depending degradation rate of the polymer and dissociation rate of the PIC micelles. This material is available free of charge via the Internet at http://pubs.acs.org.

References

(1) (a) Idota, N.; Kikuchi, A.; Kobayashi, J.; Sakai, K.; Okano, T. *Adv. Mater.* **2005**, *17*, 2723−2727. (b) Roy, I.; Gupta, M. N. *Chem. Biol.* **2003**, *10*, 1161−1171. (c) Schmaljohann, D. *Adv. Drug Delivery Rev.* **2006**, *58*, 1655−1670.
(2) (a) Lee, Y.; Koo, H.; Jin, G.; Mo, H.; Cho, M. Y.; Park, J.; Choi, J. S.; Park, J. S. *Biomacromolecules* **2005**, *6*, 24−26. (b) Miyata, K.; Kakizawa, Y.; Nishiyama, N.; Harada, A.; Yamasaki, Y.; Koyama, H.; Kataoka, K. *J. Am. Chem. Soc.* **2004**, *126*, 2355−2361.
(3) (a) Oishi, M.; Kataoka, K.; Nagasaki, Y. *Bioconjugate Chem.* **2006**, *17*, 677−688. (b) Boussif, O.; Lezoualc'h, F.; Zanta, M. A.; Mergny, M. D.; Scherman, D.; Demeneix, B.; Behr, J. P. *Proc. Natl. Acad. Sci. U.S.A.* **1995**, *92*, 7297−7301.
(4) (a) Murthy, N.; Thng, Y. X.; Schuck, S.; Xu, M. C.; Fréchet, J. M. J. *J. Am. Chem. Soc.* **2002**, *124*, 12398−12399. (b) Bae, Y.; Fukushima, S.; Harada, A.; Kataoka, K. *Angew. Chem., Int. Ed.* **2003**, *42*, 4640−4643. (c) Heller, J.; Barr, J.; Ng, S. Y.; Abdellauoi, K. S.; Gurny, R. *Adv. Drug Delivery Rev.* **2002**, *54*, 1015−1039.
(5) Shetty, J. K.; Kinsella, J. E. *Biochem. J.* **1980**, *191*, 269−272.
(6) Fukushima, S.; Miyata, K.; Nishiyama, N.; Kanayama, N.; Yamasaki, Y.; Kataoka, K. *J. Am. Chem. Soc.* **2005**, *127*, 2810.
(7) Udenfriend, S.; Stein, S.; Bohlen, P.; Dairman, W.; Leimgruber, W.; Weigele, M. *Science* **1972**, *178*, 871−872.
(8) Harada, A.; Kataoka, K. *Macromolecules* **1998**, *31*, 288−294.
(9) Harada, A.; Kataoka, K. *J. Am. Chem. Soc.* **1999**, *121*, 9241−9242.

JA071090B

Bone Regeneration by Regulated *In Vivo* Gene Transfer Using Biocompatible Polyplex Nanomicelles

Keiji Itaka[1], Shinsuke Ohba[1], Kanjiro Miyata[2], Hiroshi Kawaguchi[3], Kozo Nakamura[3], Tsuyoshi Takato[3], Ung-Il Chung[1] and Kazunori Kataoka[1,2]

[1]*Division of Clinical Biotechnology, Center for Disease Biology and Integrative Medicine, Graduate School of Medicine, The University of Tokyo, Tokyo, Japan;* [2]*Department of Materials Science and Engineering, Graduate School of Engineering, The University of Tokyo, Tokyo, Japan;* [3]*Division of Sensory and Motor System Medicine, Faculty of Medicine, The University of Tokyo, Tokyo, Japan*

Gene therapy is a promising strategy for bone regenerative medicine. Although viral vectors have been intensively studied for delivery of osteogenic factors, the immune response inevitably inhibits bone formation. Thus, safe and efficient non-viral gene delivery systems are in high demand. Toward this end, we developed a polyplex nanomicelle system composed of poly(ethyleneglycol) (PEG)-block-catiomer (PEG-b-P[Asp-(DET)]) and plasmid DNA (pDNA). This system showed little cytotoxicity and excellent transfection efficiency to primary cells. By the transfection of constitutively active form of activin receptor-like kinase 6 (caALK6) and runt-related transcription factor 2 (Runx2), the osteogenic differentiation was induced on mouse calvarial cells to a greater extent than when poly(ethylenimine) (PEI) or FuGENE6 were used; this result was due to low cytotoxicity and a sustained gene expression profile. After incorporation into the calcium phosphate cement scaffold, the polyplex nanomicelles were successfully released from the scaffold and transfected surrounding cells. Finally, this system was applied to *in vivo* gene transfer for a bone defect model in a mouse skull bone. By delivering *caALK6* and *Runx2* genes from nanomicelles incorporated into the scaffold, substantial bone formation covering the entire lower surface of the implant was induced with no sign of inflammation at 4 weeks. These results demonstrate the first success in *in vivo* gene transfer with therapeutic potential using polyplex nanomicelles.

Received 31 December 2006; accepted 30 April 2007; published online 5 June 2007. doi:10.1038/sj.mt.6300218

INTRODUCTION

Despite bone's capacity to heal spontaneously, bone repair is not always satisfactory. Approximately 5–10% of fractures do not heal well, resulting in delayed union or non-union with considerable morbidity.[1] Critical bone defects after severe trauma, tumor resection, or revision of total joint arthroplasty remain challenging problems. Autologous bone graft is considered the gold standard technique; however, it has shortcomings concerning both quantity (availability of material) and quality (donor site troubles, graft rejection, disease transmission).[2,3] These problems have heightened the need for bone regenerative medicine that uses tissue engineering techniques.[4]

A promising strategy is to combine adequate scaffolds and signals. Although some scaffolds are osteoconductive, no scaffolds invented so far are known to be osteoinductive,[5] because current scaffold materials cannot activate the signals necessary for osteogenesis. For this purpose, the potential of growth and transcriptional factors has been widely recognized.[6,7] Substantial progress has been made in the basic understanding of major osteogenic signaling molecules such as bone morphogenetic proteins (BMPs),[8] Hedgehogs,[9] Runx2,[10] Wnts,[11] and insulin-like growth factors.[12] In particular, recombinant human BMP-2 and BMP-7 have already been approved by the U.S. Food and Drug Administration for restricted clinical use. However, in spite of the remarkable findings on animal studies, clinical trials using BMP devices have not obtained comparable outcomes.[13,14] Problems such as protein stability, inadequate release profile (initial burst effect), or the need for accessory factors may have caused these inconsistent results.[6,15]

Gene therapy is a promising approach to overcome these problems. Compared with exogenous proteins, which require purification, the gene can express these bioactive factors in the native form at the regeneration site.[6] The sustained synthesis of proteins from the delivered gene can facilitate synchronization between the kinetics of signaling receptor expression and bioactive factor availability.[16] In addition, the combined use of two or more osteoinductive factors to constitute a better osteogenic signal can be evaluated with a high degree of flexibility.[17] For this purpose, viral vectors including adenovirus and adeno-associated virus vectors have been intensively studied for the delivery of the osteoinductive cytokines.[17–21] However, when these viral vectors are used, there is concern about inducing immune responses.[22] Indeed, Egermann *et al.* reported that, after a local injection of BMP-2 expressing adenoviral vector to a bone defect area in sheep, bone formation was significantly reduced even at the untreated contralateral defect area, indicating that the immune

The first two authors contributed equally to this work.

Correspondence: *Kazunori Kataoka, Department of Materials Science and Engineering, Graduate School of Engineering, The University of Tokyo, 7-3-1 Hongo, Bunkyo-ku, Tokyo 113-0033, Japan. E-mail: kataoka@bmw.t.u-tokyo.ac.jp*

response has a systemic inhibitory effect on bone formation after a single injection of adenovirus.[23]

In this context, safe and efficient non-viral gene delivery systems are in high demand. We recently developed a novel polymer-based gene delivery system that showed excellent capacity for *in vitro* transfection.[24] This system is a polyplex nanomicelle composed of poly(ethyleneglycol) (PEG)-block-polycation (PEG-b-P[Asp-(DET)]): PEG-b-polyasparagine carrying the *N*-(2-aminoethyl)aminoethyl group $(CH_2)_2NH(CH_2)_2NH_2$ as the side chain) and plasmid DNA (pDNA). The complexation of block copolymer and pDNA forms a micellar structure, and its characteristics have been found suitable for gene delivery: a diameter of ~100 nm with a PEG palisade enabling complexes to avoid foreign body recognition while providing increased nuclease resistance, increased tolerance under physiologic conditions, and excellent gene expression in a serum-containing medium.[25–27] In addition, the cationic segment of block copolymer was designed to have the buffering capacity of an acidic environment inside the endosomes as effected by the presence of unprotonated amines under neutral pH. By virtue of these features, we effectively transfected genes to culture cells with almost no cytotoxicity.[24]

We undertook the present study to investigate the feasibility of these polyplex nanomicelles for bone regenerative medicine, including the study of: (i) transfection toward various primary cells for the evaluation of efficiency and safety, (ii) induction of osteogenic differentiation by a foreign gene introduction of osteogenic factors, and (iii) *in vivo* gene transfer to a mouse bone defect model to increase the rate of bone regeneration. As will be shown, this system provides sufficient gene expression in a sustained manner both *in vitro* and *in vivo*, and it thus shows a potential therapeutic effect in a bone defect model.

RESULTS

In vitro transfection to human synovial cells

To evaluate the feasibility of polyplex nanomicelles for clinical gene therapy, *in vitro* transfection was performed toward human synovial cells derived from patients suffering from rheumatoid arthritis. By evaluating luciferase gene expression on day 2 of transfection, the polyplex nanomicelles that were formed at an optimal nitrogen/phosphate ratio showed gene expressions comparable to those of linear poly(ethylenimine) (LPEI),[28] which is well known to have excellent transfection efficiency (**Figure 1a**). At the optimal nitrogen/phosphate = 80, the polyplex nanomicelles were observed to have small absolute zeta potentials of around +10 mV (**Supplementary Figure S1**). The nanomicelles maintained appreciable gene expression even on day 5, whereas the gene expression of LPEI showed a marked decrease during the same time frame. To investigate this difference, the cytotoxicity was evaluated by a quantitative assay. Consistent with the results of gene expression, LPEI exhibited prominent cytotoxicity time-dependently (**Figure 1b**). The microscopic images following green fluorescence protein (GFP) gene transfection by LPEI showed apparent morphologic change as well as reduced numbers of cells, whereas the polyplex nanomicelles maintained almost normal phenotype concurrently with GFP expression even on day 5 (**Supplementary Figure S2**). Thus, the polyplex

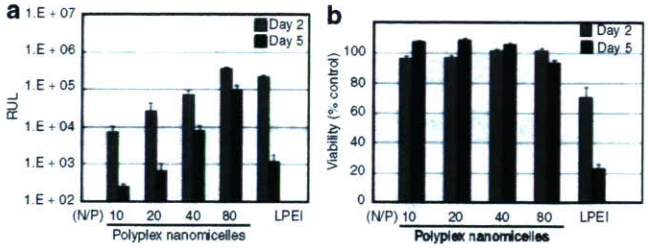

Figure 1 *In vitro* transfection to human synovial cells. (**a**) Luciferase gene expression. *In vitro* transfection of luciferase-expressing plasmid DNA was performed by polyplex nanomicelles formed at various nitrogen/phosphate (N/P) ratios and by poly(ethylenimine) (LPEI). Gene expression was evaluated after 2 and 5 days of transfection. Data are means ± SDs, $n = 4$. (**b**) Cell viability after transfection. After transfection, similar to the case in **a**, cell viability was estimated by an MTT assay. Results were expressed as the relative value (%) of the control cells, which were incubated in parallel without transfection. Data are means ± SDs, $n = 8$. RLU, relative light units.

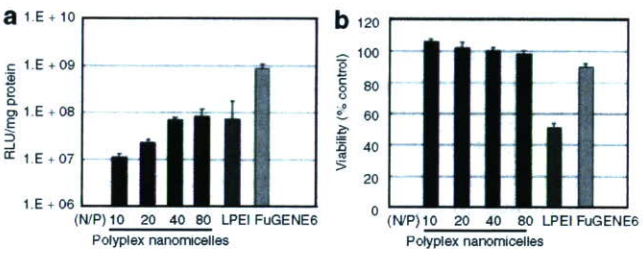

Figure 2 *In vitro* transfection to mouse calvarial cells. (**a**) Luciferase gene expression. *In vitro* transfection of luciferase-expressing plasmid DNA was performed using polyplex nanomicelles, formed at various nitrogen/phosphate (N/P) ratios, as well as poly(ethylenimine) (LPEI) and FuGENE6. Gene expression was evaluated after 2 days of transfection. Data are means ± SDs, $n = 4$. (**b**) Cell viability after transfection. After transfection, similar to the case in **a**, cell viability was estimated by an MTT assay. Results were expressed as relative values (%) of the control cells, which were incubated in parallel without transfection. Data are means ± SDs, $n = 8$. RLU, relative light units.

nanomicelles were revealed to have excellent gene transfection capacity—comparable to that of LPEI—with considerably low cytotoxicity; this suggests a great advantage for *in vivo* application.

Transfection toward mouse calvarial cells and induction of osteogenic differentiation

In applying polyplex nanomicelles to delivery genes encoding bioactive factors that activate signals necessary for osteogenesis, we evaluated the transfection capacity of foreign genes and the induction of cell differentiation toward mouse calvarial cells derived from neonatal calvariae. The evaluation of luciferase showed that gene expressions comparable to those of LPEI were obtained by polyplex nanomicelles (**Figure 2a**) without showing any cytotoxicity (**Figure 2b**). From a practical standpoint we also evaluated FuGENE6, a commercially available lipid-based transfection reagent with considerably high efficiency and biocompatibility.[29–33] With this reagent, the cells showed luciferase expression that was one order higher than with polyplex nanomicelles or LPEI and with little cytotoxicity (**Figure 2a** and **b**).

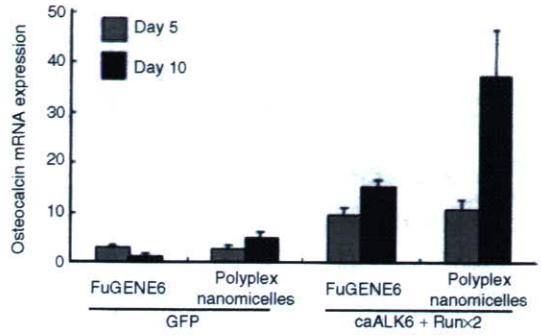

Figure 3 Evaluation of osteocalcin messenger RNA (mRNA) expression by a quantitative polymerase chain reaction (PCR). Osteogenic differentiation was induced on the mouse calvarial cells by transfection of caALK6 and Runx2 expressing plasmid DNAs. As a negative control, a green fluorescence protein (GFP) gene was also used. After 5 and 10 days, the total RNA was collected and the osteocalcin expression was quantified by a quantitative PCR. Data are means ± SDs, $n = 6$. caALK6, constitutively active form of activin receptor-like kinase 6; Runx2, runt-related transcription factor 2.

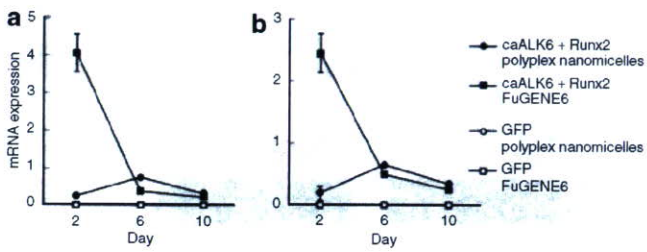

Figure 4 Evaluation of messenger RNA (mRNA) expression of (a) constitutively active form of activin receptor-like kinase 6 (caALK6) and (b) runt-related transcription factor 2 (Runx2) after transfection by a quantitative polymerase chain reaction. Two, six and ten days after transfection, the mRNA expression of ALK6 and Runx2 was quantified. Data are means ± SDs, $n = 6$. caALK6, constitutively active form of activin receptor-like kinase 6; GFP, green fluorescence protein; Runx2, runt-related transcription factor 2.

Observation of GFP expression revealed that nanomicelles and FuGENE6 achieved similar levels of gene expression without showing any morphologic changes in the cells; this is evident in the phase contrast images (**Supplementary Figure S3**).

We then investigated the osteogenic differentiation after transfection of pDNAs expressing a constitutively active form of activin receptor-like kinase 6 (caALK6) and runt-related transcription factor 2 (Runx2), which have been shown to be a potent combination of genes for bone regeneration.[34] Osteogenic differentiation was evaluated by the expression of osteocalcin messenger RNA (mRNA), an osteoblast-differentiation marker. As shown in **Figure 3**, the time-dependent increase in osteocalcin expression was confirmed after transfection of caALK6 + Runx2 by both polyplex nanomicelles and FuGENE6. Using LPEI, in contrast, osteocalcin expression was at the same level as the control cells transfected with the GFP gene (data not shown). It is interesting that, on day 10, nanomicelles showed a more remarkable increase in osteocalcin expression than did FuGENE6, although both showed comparable gene expression without cytotoxicity by the luciferase and GFP reporter assays (**Figure 2a** and **b** and

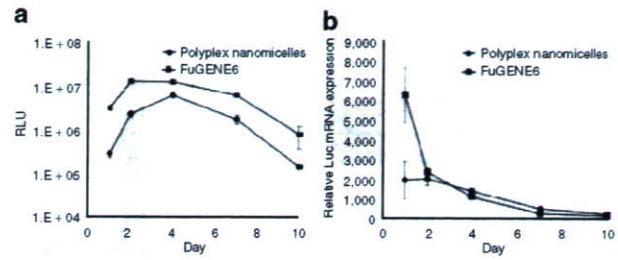

Figure 5 Evaluation of sustained expression of luciferase on mouse calvarial cells. (**a**) Luciferase expression measured by luminescence, which indicated the quantification of protein synthesis. Data are means ± SDs, $n = 12$. (**b**) Estimation of the corresponding messenger RNA (mRNA) expression by a quantitative polymerase chain reaction. For both, the mouse calvarial cells were transfected by luciferase-expressing plasmid DNA and the assays were done on days 1, 2, 4, 7, and 10. Data are means ± SDs, $n = 6$. RLU, relative light units.

Supplementary Figure S3). It is reasonable to assume that, with the same transfection procedure as used with the reporter genes, *caALK6* and *Runx2* were also expressed similarly by nanomicelles and FuGENE6. The reasons for this disparity in osteocalcin induction are unclear, but FuGENE6 may cause some appendant effect on cell differentiation that is difficult to detect by a nonspecific viability evaluation such as the MTT assay.[35] Regarding this concern we speculated that, since the difference was visible on day 10, the expression profile of the transfected genes might differ between nanomicelles and FuGENE6, thus affecting the outcome of the induction of cell differentiation.

To investigate this possibility, the time-dependent change of gene expression was quantified. As shown in **Figure 4**, the mRNA expressions of caALK6 and Runx2 showed similar profiles, where FuGENE6 initially induced expressions of ALK6 and Runx2 that were one order higher than nanomicelles, although the expressions sharply decreased with time. In contrast, the nanomicelles showed rather consistent gene expressions. For a detailed investigation, the luciferase gene was used and the protein systhesis and its mRNA expression were simultaneously quantified by a luminescence measurement and a quantitative polymerase chain reaction (PCR), respectively. As shown in **Figure 5**, FuGENE6 initially showed light emission (indicating the amount of synthesized protein) that was one order higher than did the nanomicelles. The highest expression was obtained on day 2. The initial mRNA expression was always high, but a rapid decrease was observed after day 2. In contrast, the polyplex nanomicelles showed fairly consistent gene expression profiles, giving the highest luciferase expression on day 4 and with sustained mRNA expression thereafter. Because cell differentiation would require some processes in signaling pathways inside the cells, it follows that such a continuous manner of gene expression by polyplex nanomicelles might contribute to the efficient induction of differentiation. Hence, the nanomicelle profile is a promising feature for *in vivo* bone regeneration.

In vitro transfection from gene-containing scaffolds

The *in vivo* gene transfer to a bone regeneration site should require the retention and gradual release of gene carriers. One promising approach is to incorporate the carriers into implantable scaffolds.

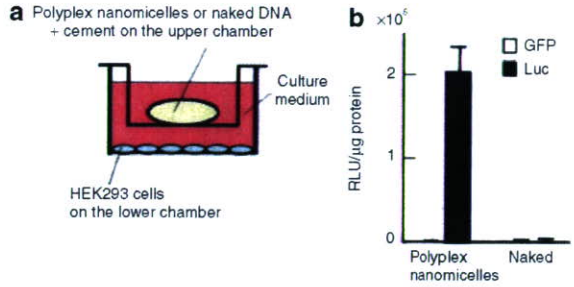

Figure 6 *In vitro* transfection by polyplex nanomicelles incorporated into calcium phosphate cement scaffold. **(a)** Schematic illustration of the *in vitro* transfection from the gene-containing scaffolds. The scaffold containing polyplex nanomicelles of PEG-b-P[Asp-(DET)] and plasmid DNA (pDNA) expressing luciferase gene or naked pDNA was plated onto the upper chamber of cell culture insert, and the HEK293 cells were plated onto the lower chamber. **(b)** Luciferase expression in HEK293 cells. After 5 days of transfection, luciferase expression was measured. The green fluorescence protein (GFP) gene was used as a negative control. Data are means ± SDs, $n = 3$. DET, diethylenetriamine; PEG, poly(ethyleneglycol); RLU, relative light units.

This form of gene delivery is called the gene-activated matrix, through which Bonadio *et al.* pioneered the incorporation of non-viral vectors in collagen scaffolds to stimulate bone formation in a rat defect model.[36] In this study, the polyplex nanomicelles were incorporated into a calcium phosphate cement scaffold by mixing. This process is highly biocompatible, bioactive (especially in bone tissue), moldable, and injectable.

In order to investigate whether or not the polyplex nanomicelles containing luciferase-expressing pDNA were delivered from the calcium phosphate cement scaffold, the scaffold was put into the culture medium of HEK293 cells for 5 days. The cement and the cells were physically separated by a filter to avoid direct contact between the cement and the cells, which could hinder the distinction between the release and the direct delivery of polyplex nanomicelles from the scaffold (**Figure 6**). As shown in **Figure 6b**, the cells cultured with the scaffold containing the polyplex nanomicelles exhibited apparent luciferase expression, whereas the cells cultured with the scaffold containing naked pDNA did not. Thus, the polyplex nanomicelles incorporated into the calcium phosphate cement scaffold successfully introduced the contained genes into the surrounding cells.

Next, to investigate how long the transfection by polyplex nanomicelles incorporated into the scaffold would last, the scaffold was placed on the culture dish and then mouse calvarial cells were plated on top of it and cultured for an extended period. Monitoring of luminescence using the IVIS Imaging System (Xenogen, Alameda, CA) revealed that the gene expression of mouse calvarial cells by the scaffold containing polyplex nanomicelles with luciferase-expressing pDNA increased, peaking near days 10 and 18, and then gradually declined to the background level approaching day 25 (**Supplementary Figure S4a**). Quantitative visualization of luminescence using this imaging system revealed that cells on top of the scaffold and in its close proximity were first transfected at days 2 and 10; subsequently, cells at some distance were transfected until day 25 (**Supplementary Figure S4b**). Thus, the polyplex nanomicelles incorporated into the scaffold delivered genes in a sustained manner.

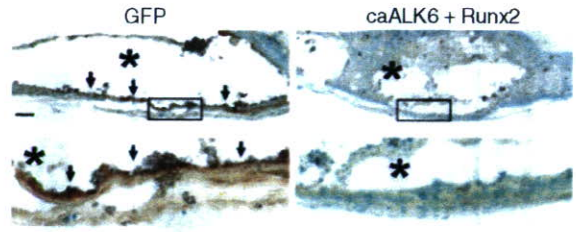

Figure 7 *In vivo* gene transfer by polyplex nanomicelles. Immunohistochemistry for green fluorescence protein (GFP) of calvarias implanted with the scaffold containing polyplex nanomicelles of PEG-b-P[Asp-(DET)] and plasmid DNA expressing GFP or caALK6 + Runx2 at 4 weeks after implantation. GFP protein was stained brown (arrows). The lower panel of each group shows a magnified view of the boxed area in the upper panel. Asterisks denote the remnants of calcium phosphate pastes. Scale bar: 200 μm. caALK6, constitutively active form of activin receptor-like kinase 6; DET, diethylenetriamine; PEG, poly(ethyleneglycol); Runx2, runt-related transcription factor 2.

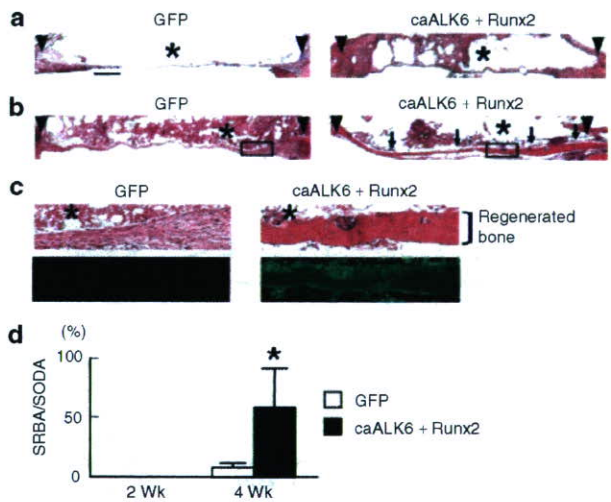

Figure 8 Bone regeneration by polyplex nanomicelles. **(a, b)** Histologic analyses of calvarias. The scaffold containing polyplex nanomicelles of PEG-b-P[Asp-(DET)] and plasmid DNA expressing green fluorescence protein (GFP) or caALK6 + Runx2 was implanted on the bone defect area on the mouse skull bone. At **(a)** 2 weeks and **(b)** 4 weeks after implantation, histologic and immunohistologic analyses were performed. Sections were stained with hematoxylin and eosin (H&E). Arrowheads denote defect edges; arrows, regenerated bones; asterisks, the remnants of calcium phosphate cement. Scale bar: 500 μm. **(c)** Magnified views of boxed areas in **b**. H&E (bright field views) and immunohistochemstry for type-I collagen (dark field views) were performed on serial sections. Green fluorescence indicates expression of type-I collagen. Asterisks, the remnants of calcium phosphate cement. **(d)** Quantification of bone regeneration. The ratio of the summation of the regenerated bone area to that of the original defect area (SRBA/SODA) in designated sections was histologically measured by NIH Image software. Data are means ± SD of five mice per group. *$P < 0.01$ versus GFP at 4 weeks after implantation. caALK6, constitutively active form of activin receptor-like kinase 6; DET, diethylenetriamine; PEG, poly(ethyleneglycol); Runx2, runt-related transcription factor 2.

In vivo gene delivery to the bone defect area on the mouse calvarial bone

The data so far have shown that a localized and sustained system to deliver polyplex nanomicelles was successfully developed *in vitro* using the calcium phosphate cement scaffold. To

investigate whether or not this system is effective for *in vivo* gene delivery, the scaffold was molded to the fitting shape and implanted in mouse calvarial bone defects. After implantation of the scaffold containing polyplex nanomicelles with GFP pDNA, successfully transfected recipient cells were observed across a few layers from the implant surface by immunohistochemical analyses (**Figure 7**). The intensity of the staining was strongest in cells immediately adjacent to the scaffold, gradually declining with distance.

To investigate the therapeutic potential of this system, polyplex nanomicelles containing pDNAs expressing a caALK6 and Runx2, by which the osteogenic differentiation was induced on the calvarial cells *in vitro* (**Figure 3**), were incorporated into the calcium phosphate cement scaffold and implanted in the same model. At 2 weeks after implantation, no bone formation occurred in either the control group transfected with the GFP-expressing pDNA or the treatment group transfected with caALK6 + Runx2 expressing pDNA (**Figure 8a**). At 4 weeks after implantation, however, substantial bone formation covering the entire lower surface of the implant was induced only in the treatment group (**Figure 8b**), as confirmed by the quantitative analysis of the regenerated bone area (**Figure 8d**). The regenerated bone tissues exhibited a lamellar structure containing osteocyte-like cells and strongly expressed the type-I collagen protein (**Figure 8c**). On the other hand, the incorporation of neither the LPEI nor the FuGENE6 complex into the calcium phosphate cement scaffold generated any apparent bone formation at 4 weeks (data not shown). It should be noted that no sign of inflammation was observed in any group (**Figure 8a–c**). The results so far indicate that the polyplex nanomicelles incorporated into the calcium phosphate cement scaffold transfected the foreign genes to the cells in the vicinity of the scaffold, leading to a considerable increase in the rate of bone formation via the induction of osteogenic differentiation.

DISCUSSION

Many clinical fields demand useful non-viral gene delivery systems that satisfy high standards of both efficacy of gene introduction and low toxicity.[37] Bone tissue engineering would be a promising field; however, only a few trials have been reported so far. Bright *et al.* used a naked pDNA expressing OP-1 (BMP-7) gene, which was incorporated into a collagen scaffold, for a rat model of lumbar interbody arthrodesis.[38] Although bone formation was stimulated after 4 weeks, it was not as extensive as that observed after the injection of recombinant human OP-1 protein, in spite of considerably high dose of pDNA (250 μg/rat). Huang *et al.* combined poly(lactic-co-glycolic acid) scaffolds with 200 μg of condensed pDNA encoding BMP4 using branched PEI and implanted the scaffolds into rat cranial defects.[39] They successfully induced bone regeneration at the defect edges; however, osteoid and mineralized tissue was significantly increased after 15 weeks of implantation. The disparity between our results and theirs presumably resulted from the difference in the osteogenic signals. However, some toxic effects of PEI should also be taken into consideration: PEI was reported to be an apoptotic agent,[40] and indeed in our results it showed appreciable cytotoxicity (**Figures 1b** and **2b**) and an inability to induce differentiation. Directly comparing the capacity of their versus our method was not possible because Huang *et al.* did not provide data on the actual transfection efficiency; however, some negative effects of PEI on the cells in the vicinity of the scaffold may have caused the delayed induction of bone regeneration.

The considerably low dose of pDNA (1.3 μg/mouse) is also characteristic in our system. In previous studies of *in vivo* bone formation by non-viral gene delivery systems, a larger amount of pDNA (100 μg to 1 mg) was used.[38,39,41] We assume that this may be attributed to the capacity of polyplex nanomicelles to stably retain pDNA even in the scaffolds. Moreover, using the combination of osteogenic genes *caALK6* and *Runx2* contributed to the efficient osteoconductivity of our system. The cooperative action of this combination occurred through protein stabilization of core binding factor beta (Cbfb) and through induction of Runx2–Cbfb complex formation and its DNA binding, leading to the efficient induction of osteogenic differentiation.[34]

FuGENE6 has often been reported to have excellent transfection efficiency *in vitro*, including the induction of cell differentiation.[29–33] Indeed, in our results shown in **Figure 3**, comparable induction of osteocalcin expression was observed by both FuGENE6 and polyplex nanomicelles on day 5. It is interesting to note that, although the gene expressions evaluated by luciferase were consistently higher in FuGENE6 until day 10 (**Figure 5**), the osteocalcin induction was more remarkable in the nanomicelles on day 10 (**Figure 3**). The marked difference in gene expression profiles between nanomicelles and FuGENE6—especially when evaluated by mRNA expression—might influence the outcome of cell differentiation, which requires complex intracellular processes over an extended period. It is also possible that some toxicologic effects of the reagents might influence the cell reactivity, since many lipid-based transfection reagents were reported to induce changes in the expression of endogenous genes.[42] The study of toxicologic or pharmacologic effects of bioactive materials that might alter responses to delivered drugs or genes is now attracting attention as polymer (material) genomics.[43] From this standpoint, we have started comprehensive analyses of cell bioactivities after various transfection procedures, including the study of endogenous gene expression profiles using complementary DNA arrays. These results will be reported elsewhere in the near future.

The polyplex nanomicelles composed of PEG-b-P[Asp-(DET)] block copolymer and pDNA have demonstrated promising features for bone-regenerative gene therapy. The characteristics are summarized as: (i) good transfection efficiency with minimal cytotoxicity; (ii) sustained gene expression profile, which may be beneficial to cell differentiation; and (iii) excellent *in vivo* availability. Worth noting is that the enhancement of bone regeneration in this study was achieved without cell transplantation. Although the use of cell sources such as stem cells has been widely investigated, there remain many concerns for clinical application, such as the difficulty of finding an ideal cell source that meets both quality and quantity demands while also satisfying the concerns of medical costs and health risks.[44,45] Thus, it is desirable that cell transplantation be supplemented or replaced by innovations in other components of tissue engineering, signals, and scaffolds.

In conclusion, we developed a new gene delivery system applicable to bone regenerative medicine. This polyplex nanomicelle showed high biocompatibility as well as a capacity for regulated gene transfer, inducing a remarkable increase in the bone regeneration rate in a bone defect model. This system holds much promise for constructing a practical gene-activated matrix for tissue engineering. Moreover, this technology will help realize therapeutic applications of gene therapy requiring safe and regulated gene expressions.

MATERIALS AND METHODS

Materials. pDNAs encoding luciferase (pGL3-control, 5,256 bp) (Promega, Madison, WI) and GFP (pEGFP-C1, 4,700 bp) (Clontech, Palo Alto, CA) were amplified in competent DH5α *Escherichia coli* and purified using EndoFree Plasmid Maxi or Mega Kits (Qiagen, Hilden, Germany). pCMV5 pDNA expressing hemagglutinin-tagged mouse caALK6 and pcDEF3 pDNA expressing Flag-tagged mouse Runx2 were generous gifts from M. Krüppel (Mt. Sinai Hospital, Toronto, Canada) and K. Miyazono (University of Tokyo, Tokyo, Japan), respectively. The DNA concentration was determined by reading the absorbance at 260 nm. Commercially available transfection reagents, linear polyethylenimine (Exgen 500, M_w of LPEI = 22 kd) and FuGENE6 were purchased from MBI Fermentas (Burlington, Canada) and Roche (Basel, Switzerland), respectively. Dulbecco's modified Eagle's medium and fetal bovine serum were purchased from Sigma-Aldrich (St. Louis, MO).

Synthesis and characterization of PEG-b-P[Asp-(DET)] block copolymer. The PEG-b-P[Asp-(DET)] block copolymer was synthesized as previously reported.[24] Briefly, PEG-poly(β-benzyl-L-aspartate) (PEG-PBLA) diblock copolymer was synthesized by the ring-opening polymerization of β-benzyl-L-aspartate *N*-carboxy-anhydride from the terminal primary amino group of α-methoxy-ω-amino PEG (M_w: 12,000; Nippon Oil and Fats, Tokyo, Japan). The copolymer thus prepared was confirmed to be unimodal with a narrow molecular weight distribution (M_w/M_n: 1.23) by gel-permeation chromatography, and the number of repeating units of BLA was calculated to be 68 by ^{1}H-NMR (data not shown). The N-terminal amino group of PEG-PBLA was then acetylated using acetic anhydride in dichloromethane solution to obtain PEG-PBLA-Ac. The obtained polymer was dissolved in distilled *N,N*-dimethylformamide (Wako Pure Chemical Industries, Osaka, Japan) and reacted with diethylenetriamine (DET) (Tokyo Kasei Kogyo, Tokyo, Japan) for 24 hours at 40 °C under a dry argon atmosphere to undergo aminolysis of the benzyl side chain. After 24 hours, the solution was slowly dropped into 10% acetic acid solution and dialyzed (Spectra/por Membrane, molecular weight cut-off = 3,500, Rancho Dominquez, CA) against 0.01 N HCl and subsequently against distilled water. The final solution was lyophilized to obtain PEG-b-P[Asp-(DET)] as the hydrochloride salt form. ^{1}H-NMR confirmed the complete substitution of benzyl ester of the polymer with DET through the aminolysis reaction as well as the chemical structure of the obtained PEG-b-P[Asp-(DET)] block copolymer.

Preparation of pDNA carriers. The PEG-b-P[Asp-(DET)] block copolymer and pDNA were separately dissolved in 10 mmol/l Tris-HCl buffer (pH 7.4). Both solutions were mixed at various nitrogen/phosphate (= (total amines in cationic segment)/(DNA phosphates)) and left overnight. The pDNA complexes with LPEI and FuGENE6 were prepared by mixing the pDNA solution and the reagents following the protocols provided by the manufacturers.

In vitro *transfection.* HEK293 cells were obtained from the Riken Cell Bank (Tsukuba, Japan). Mouse calvarial cells were isolated from calvariae of neonatal littermates. The experimental procedures were in accordance with the guidelines of the Animal Committee of the University of Tokyo. Calvariae were digested for 10 minutes at 37 °C in an enzyme solution containing 0.1% collagenase and 0.2% dispase for five cycles. Cells isolated by the final four digestions were combined as an osteoblast population and cultured in Dulbecco's modified Eagle's medium containing 10% fetal bovine serum. Human synovial cells from rheumatoid arthritis patients were kindly provided by Dr. S. Tanaka (University of Tokyo).[46] Written informed consent for subsequent experiments was obtained from each patient.

For luciferase transfection assays, the cells were inoculated at a density of 2×10^4 cells/well in a 24-multiwell plate and cultured for 24 hours. After the culture medium was replaced with fresh medium containing 10% fetal bovine serum, pDNA carrier solution (33.3 μg/ml, 22.5 ml) was applied to each well. After several days of incubation, the cells were lysed and the luciferase gene expression was measured using a Luciferase Assay System (Promega, Madison, WI) and a Lumat LB9507 luminometer (Berthold, Bad Wildbad, Germany). The expression was normalized to protein concentrations of cell lysates. For the evaluation of sustained luciferase expression (**Figure 4**), the cells were seeded onto a 96-multiwell plate (6×10^3 cells/well). After incubation for 24 hours, 6 μl of each pDNA carrier solution was added, followed by further incubation for up to day 10. The luminescence was measured by a GloMax 96 Microplate Luminometer (Promega, Madison, WI). For the GFP transfection assay, both the phase contrast and the fluorescence images were obtained by an Axiovert 100 M microscope (Carl Zeiss, Oberkochen, Germany).

For the cytotoxicity assay, a 96-multiwell plate was used. After transfection as described above, the cells were incubated for 2 or 5 days and their viability was evaluated by an MTT assay (Cell Counting Kit-8, Dojindo, Kumamoto, Japan). Each well was measured by reading the absorbance at 450 nm according to the protocol provided by the manufacturer. The results were expressed as the relative value (%) of the control cells, which were incubated in parallel without transfection.

Evaluation of mRNA expression. After transfection to mouse calvarial cells, the total RNA was collected using the RNeasy Mini Preparation Kit (Qiagen, Hilden, Germany) according to the manufacturer's protocol. Gene expression was analyzed by quantitative PCR. Using the Quantitect SYBR Green PCR Kit (Qiagen, Hilden, Germany), 20 ng of total RNA was analyzed in a final volume of 20 μl according to the manufacturer's protocol. Reverse transcription was performed for 30 minutes at 50 °C followed by PCR: 40 thermal cycles of 15 seconds at 94 °C, 30 seconds at 55 °C, and 30 seconds at 72 °C using an ABI Prism 7500 Sequence Detector (Applied Biosystems, Foster City, CA). Each mRNA expression was normalized to levels of mouse β-actin mRNA, also determined by quantitative reverse transcription-PCR, from the same total RNA samples. The following primers were used: osteocalcin, forward primer (AAGCAGGAGGGC AATAAGGT) and reverse primer (TTTGTAGGCGGTCTTCAAGC); mouse ALK6, forward primer (CACCAAGAAGGAGGATGGAG) and reverse primer (CTAGACATCCAGAGGTGACAACAG); mouse Runx2, forward primer (CCCAGCCACCTTTACCTACA) and reverse primer (TATGGAGTGCTGCTGGTCTG); luciferase, forward primer (TTGA CCGCCTGAAGTCTCTGA) and reverse primer (ACACCTGCGTCGA AGATGTTG); mouse β-actin, forward primer (AGATGTGGATCAG CAAGCAG) and reverse primer (GCGCAAGTTAGGTTTTGTCA). As for luciferase, the gene expression presented as the light units was also evaluated in parallel.

In vitro *transfection from gene-containing scaffolds.* To prepare the scaffolds containing gene carriers, the PEG-P[Asp-(DET)]/pDNA micelles were mixed with calcium phosphate paste (BIOPEX-R; Mitsubishi Pharma, Osaka, Japan). According to the manufacturer's information, the powder consists of particles (2–5 mm in diameter) of α-tricalcium phosphate (75% wt), tetracalcium phosphate monoxide (18% wt), dicalcium phosphate dibasic (5% wt), and hydroxyapatite (2% wt); the aqueous solution contains sodium chondroitin sulfate (5.4%) and sodium succinate

(13%). For solidification, 1.0 g of the powder was manually mixed (at low shear rates) with 233 μl of the solution containing pDNAs. After solidification, the cement containing 1.3 μg of pDNA was placed onto the upper chamber of a BD Falcon Cell Culture Insert for 12-well plates (1.0 μm pore size, Becton Dickinson, Franklin Lakes, NJ), and HEK293 cells were plated onto the lower chamber. Five days later, luciferase assay was performed as described. The level of luciferase expression was normalized to the protein concentrations of cell lysates.

In vivo *gene delivery for the bone defect area on the mouse skull bone.* In this study, the 4 mm defects in diameter were chosen as the mouse bone defect model.[47,48] We have observed that the mouse calvarial defects (4 mm in diameter) could not be covered spontaneously with regenerated bone within 8 weeks after operation, although significant bone formation was observed at the defect edge (data not shown). Thus, the bone regeneration was evaluated within or at 4 weeks after gene delivery.

For the generation of bone defects, mice were anesthetized with ketamine/xylazine (80 mg/kg and 5 mg/kg) solution through intraperitoneal injection, and a linear incision was made along the sagittal suture from the frontal bone to the center of the occipital bone. A round craniotomy defect (4 mm in diameter) was manually created on both parietal bones with a sterile disposable trephine (Kai Industries, Gifu, Japan).[47] Calcium phosphate paste was used to fill in the defects, and then the incisions were sutured. The mice were killed at 2, 4, or 8 weeks after the operation for radiologic, histologic, or immunohistologic analyses, respectively. Animal experiments were performed according to the protocol approved by the Animal Care and Use Committee of the University of Tokyo.

Assessment of bone regeneration. After the mice were asphyxiated with carbon dioxide, the calvarias were removed. Tissue preparation, hematoxylin and eosin staining, and immunohistologic analysis using a rabbit polyclonal antibody against GFP (Molecular Probes, Eugene, OR) or a rabbit polyclonal antibody against type-I collagen (LSL, Tokyo, Japan) were performed as described.[49] To evaluate the extent of bone regeneration, serial coronal sections of the implantation site were performed at 0.5, 1, 1.5, 2, 2.5, 3, and 3.5 mm from the rostral end and then stained with hematoxylin and eosin. For each section, the original defect area and the regenerated bone area were measured by NIH Image software. The ratio of the summation of the regenerated bone area to that of the original defect area (SRBA/SODA) was calculated and used as the index of bone regeneration.

ACKNOWLEDGMENTS

We thank Michael Klüppel (Mount Sinai Hospital) and Kohei Miyazono (University of Tokyo) for pDNAs expressing caALK6 and Runx2, respectively. We also appreciate Sakae Tanaka (University of Tokyo) for providing human synovial cells. This work was supported by Grants-in-Aid for Scientific Research from the Japanese Ministry of Education, Culture, Sports, Science and Technology (#15390452 and #17390530), Health Science Research Grants from the Japanese Ministry of Health, Labor and Welfare (#H16-regenerative medicine-008), and the Core Research Program for Evolutional Science and Technology (CREST) from the Japan Science and Technology Corporation (JST).

SUPPLEMENTARY MATERIAL

Figure S1. Zeta-potential of polyplex nanomicelles and pDNA complexes with P[Asp-(DET)], the cationic segment of the block copolymer used in this study.

Figure S2. GFP gene expression in human synovial cells.

Figure S3. GFP gene expression in mouse calvarial cells.

Figure S4. *In vitro* transfection by polyplex nanomicelles incorporated into calcium phosphate cement scaffold.

REFERENCES

1. Bucholz, RW, Heckman, JD (2006). *Rockwood and Green's Fractures in Adults*. Lippincott Williams & Wilkins: Philadelphia, PA. 587pp.
2. Banwart, JC, Asher, MA and Hassanein, RS (1995). Iliac crest bone graft harvest donor site morbidity. A statistical evaluation. *Spine* **20**: 1055–1060.
3. Arrington, ED, Smith, WJ, Chambers, HG, Bucknell, AL and Davino, NA (1996). Complications of iliac crest bone graft harvesting. *Clin Orthop Relat Res* **329**: 300–309.
4. Langer, R and Vacanti, JP (1993). Tissue engineering. *Science* **260**: 920–926.
5. Bruder, SP and Caplan, AI (2000). *Principles of Tissue Engineering*. Academic Press: San Diego, CA. 683pp.
6. Winn, SR, Hu, Y, Sfeir, C and Hollinger, JO (2000). Gene therapy approaches for modulating bone regeneration. *Adv Drug Deliv Rev* **42**: 121–138.
7. Baltzer, AW and Lieberman, JR (2004). Regional gene therapy to enhance bone repair. *Gene Ther* **11**: 344–350.
8. Katagiri, T and Takahashi, N (2002). Regulatory mechanisms of osteoblast and osteoclast differentiation. *Oral Dis* **8**: 147–159.
9. Long, F, Chung, UI, Ohba, S, McMahon, J, Kronenberg, HM and McMahon, AP (2004). Ihh signaling is directly required for the osteoblast lineage in the endochondral skeleton. *Development* **131**: 1309–1318.
10. Komori, T (2003). Requisite roles of Runx2 and Cbfb in skeletal development. *J Bone Miner Metab* **21**: 193–197.
11. Patel, MS and Karsenty, G (2002). Regulation of bone formation and vision by LRP5. *N Engl J Med* **346**: 1572–1574.
12. Ogata, N, Chikazu, D, Kubota, N, Terauchi, Y, Tobe, K, Azuma, Y *et al.* (2000). Insulin receptor substrate-1 in osteoblast is indispensable for maintaining bone turnover. *J Clin Invest* **105**: 935–943.
13. Govender, S, Csimma, C, Genant, HK, Valentin-Opran, A, Amit, Y, Arbel, R *et al.* (2002). Recombinant human bone morphogenetic protein-2 for treatment of open tibial fractures: a prospective, controlled, randomized study of four hundred and fifty patients. *J Bone Joint Surg Am* **84-A**: 2123–2134.
14. Valentin-Opran, A, Wozney, J, Csimma, C, Lilly, L and Riedel, GE (2002). Clinical evaluation of recombinant human bone morphogenetic protein-2. *Clin Orthop Relat Res* **395**: 110–120.
15. Gerstenfeld, LC, Cullinane, DM, Barnes, GL, Graves, DT and Einhorn, TA (2003). Fracture healing as a post-natal developmental process: molecular, spatial, and temporal aspects of its regulation. *J Cell Biochem* **88**: 873–884.
16. Howell, TH, Fiorellini, J, Jones, A, Alder, M, Nummikoski, P, Lazaro, M *et al.* (1997). A feasibility study evaluating rhBMP-2/absorbable collagen sponge device for local alveolar ridge preservation or augmentation. *Int J Periodontics Restorative Dent* **17**: 124–139.
17. Zhao, M, Zhao, Z, Koh, JT, Jin, T and Franceschi, RT (2005). Combinatorial gene therapy for bone regeneration: cooperative interactions between adenovirus vectors expressing bone morphogenetic proteins 2, 4, and 7. *J Cell Biochem* **95**: 1–16.
18. Riew, KD, Wright, NM, Cheng, S, Avioli, LV and Lou, J (1998). Induction of bone formation using a recombinant adenoviral vector carrying the human BMP-2 gene in a rabbit spinal fusion model. *Calcif Tissue Int* **63**: 357–360.
19. Rutherford, RB, Moalli, M, Franceschi, RT, Wang, D, Gu, K and Krebsbach, PH (2002). Bone morphogenetic protein-transduced human fibroblasts convert to osteoblasts and form bone *in vivo*. *Tissue Eng* **8**: 441–452.
20. Schek, RM, Hollister, SJ and Krebsbach, PH (2004). Delivery and protection of adenoviruses using biocompatible hydrogels for localized gene therapy. *Mol Ther* **9**, 130–138.
21. Gafni, Y, Pelled, G, Zilberman, Y, Turgeman, G, Apparailly, F, Yotvat, H *et al.* (2004). Gene therapy platform for bone regeneration using an exogenously regulated, AAV-2-based gene expression system. *Mol Ther* **9**: 587–595.
22. Lundstrom, K (2003). Latest development in viral vectors for gene therapy. *Trends Biotechnol* **21**: 117–122.
23. Egermann, M, Lill, CA, Griesbeck, K, Evans, CH, Robbins, PD, Schneider, E *et al.* (2006). Effect of BMP-2 gene transfer on bone healing in sheep. *Gene Ther* **13**: 1290–1299.
24. Kanayama, N, Fukushima, S, Nishiyama, N, Itaka, K, Jang, WD, Miyata, K *et al.* (2006). A PEG-based biocompatible block catiomer with high buffering capacity for the construction of polyplex micelles showing efficient gene transfer toward primary cells. *ChemMedChem* **1**: 439–444.
25. Harada-Shiba, M, Yamauchi, K, Harada, A, Takamisawa, I, Shimokado, K and Kataoka, K (2002). Polyion complex micelles as vectors in gene therapy—pharmacokinetics and *in vivo* gene transfer. *Gene Ther* **9**: 407–414.
26. Itaka, K, Harada, A, Nakamura, K, Kawaguchi, H and Kataoka, K (2002). Evaluation by fluorescence resonance energy transfer of the stability of nonviral gene delivery vectors under physiological conditions. *Biomacromolecules* **3**: 841–845.
27. Itaka, K, Yamauchi, K, Harada, A, Nakamura, K, Kawaguchi, H and Kataoka, K (2003). Polyion complex micelles from plasmid DNA and poly(ethylene glycol)-poly(L-lysine) block copolymer as serum-tolerable polyplex system: physicochemical properties of micelles relevant to gene transfection efficiency. *Biomaterials* **24**: 4495–4506.
28. Boussif, O, Lezoualc'h, F, Zanta, MA, Mergny, MD, Scherman, D, Demeneix, B *et al.* (1995). A versatile vector for gene and oligonucleotide transfer into cells in culture and *in vivo*: polyethylenimine. *Proc Natl Acad Sci USA* **92**: 7297–7301.
29. Hellgren, I, Drvota, V, Pieper, R, Enoksson, S, Blomberg, P, Islam, KB *et al.* (2000). Highly efficient cell-mediated gene transfer using non-viral vectors and FuGene6: *in vitro* and *in vivo* studies. *Cell Mol Life Sci* **57**: 1326–1333.
30. Weiskirchen, R, Kneifel, J, Weiskirchen, S, van de Leur, E, Kunz, D and Gressner, AM (2000). Comparative evaluation of gene delivery devices in primary cultures of rat hepatic stellate cells and rat myofibroblasts. *BMC Cell Biol* **1**: 4.
31. Lee, MJ, Cho, SS, You, JR, Lee, Y, Kang, BD, Choi, JS *et al.* (2002). Intraperitoneal gene delivery mediated by a novel cationic liposome in a peritoneal disseminated ovarian cancer model. *Gene Ther* **9**: 859–866.
32. Elmadbouh, I, Rossignol, P, Meilhac, O, Vranckx, R, Pichon, C, Pouzet, B *et al.* (2004). Optimization of *in vitro* vascular cell transfection with non-viral vectors for *in vivo* applications. *J Gene Med* **6**: 1112–1124.
33. Tinsley, RB, Faijerson, J and Eriksson, PS (2006). Efficient non-viral transfection of adult neural stem/progenitor cells, without affecting viability, proliferation or differentiation. *J Gene Med* **8**: 72–81.
34. Ohba, S, Ikeda, T, Kugimiya, F, Yano, F, Lichtler, AC, Nakamura, K *et al.* (2007). Identification of a potent combination of osteogenic genes for bone

regeneration using embryonic stem (ES) cell-based sensor. *FASEB J* (epub ahead of print).
35. Hunter, AC (2006). Molecular hurdles in polyfectin design and mechanistic background to polycation induced cytotoxicity. *Adv Drug Deliv Rev* **58**: 1523–1531.
36. Bonadio, J, Smiley, E, Patil, P and Goldstein, S (1999). Localized, direct plasmid gene delivery *in vivo*: prolonged therapy results in reproducible tissue regeneration. *Nat Med* **5**: 753–759.
37. Verma, IM and Somia, N (1997). Gene therapy—promises, problems and prospects. *Nature* **389**: 239–242.
38. Bright, C, Park, YS, Sieber, AN, Kostuik, JP and Leong, KW (2006). *In vivo* evaluation of plasmid DNA encoding OP-1 protein for spine fusion. *Spine* **31**: 2163–2172.
39. Huang, YC, Simmons, C, Kaigler, D, Rice, KG and Mooney, DJ (2005). Bone regeneration in a rat cranial defect with delivery of PEI-condensed plasmid DNA encoding for bone morphogenetic protein-4 (BMP-4). *Gene Ther* **12**: 418–426.
40. Moghimi, SM, Symonds, P, Murray, JC, Hunter, AC, Debska, G and Szewczyk, A (2005). A two-stage poly(ethylenimine)-mediated cytotoxicity: implications for gene transfer/therapy. *Mol Ther* **11**: 990–995.
41. Geiger, F, Bertram, H, Berger, I, Lorenz, H, Wall, O, Eckhardt, C *et al.* (2005). Vascular endothelial growth factor gene-activated matrix (VEGF165-GAM) enhances osteogenesis and angiogenesis in large segmental bone defects. *J Bone Miner Res* **20**: 2028–2035.
42. Omidi, Y, Hollins, AJ, Benboubetra, M, Drayton, R, Benter, IF and Akhtar, S (2003). Toxicogenomics of non-viral vectors for gene therapy: a microarray study of lipofectin- and oligofectamine-induced gene expression changes in human epithelial cells. *J Drug Target* **11**: 311–323.
43. Kabanov, AV, Batrakova, EV, Sriadibhatla, S, Yang, Z, Kelly, DL and Alakov, VY (2005). Polymer genomics: shifting the gene and drug delivery paradigms. *J Control Release* **101**: 259–271.
44 Buttery, LD, Bourne, S, Xynos, JD, Wood, H, Hughes, FJ, Hughes, SP *et al.* (2001). Differentiation of osteoblasts and *in vitro* bone formation from murine embryonic stem cells. *Tissue Eng* **7**: 89–99.
45. Jiang, Y, Vaessen, B, Lenvik, T, Blackstad, M, Reyes, M and Verfaillie, CM (2002). Multipotent progenitor cells can be isolated from postnatal murine bone marrow, muscle, and brain. *Exp Hematol* **30**: 896–904.
46. Seto, H, Kamekura, S, Miura, T, Yamamoto, A, Chikuda, H, Ogata, T *et al.* (2004). Distinct roles of Smad pathways and p38 pathways in cartilage-specific gene expression in synovial fibroblasts. *J Clin Invest* **113**: 718–726.
47. Hirata, K, Tsukazaki, T, Kadowaki, A, Furukawa, K, Shibata, Y, Moriishi, T *et al.* (2003). Transplantation of skin fibroblasts expressing BMP-2 promotes bone repair more effectively than those expressing Runx2. *Bone* **32**: 502–512.
48. Cowan, CM, Shi, YY, Aalami, OO, Chou, YF, Mari, C, Thomas, R *et al.* (2004). Adipose-derived adult stromal cells heal critical-size mouse calvarial defects. *Nat Biotechnol* **22**: 560–567.
49. Kugimiya, F, Kawaguchi, H, Kamekura, S, Chikuda, H, Ohba, S, Yano, F *et al.* (2005). Involvement of endogenous bone morphogenetic protein (BMP) 2 and BMP6 in bone formation. *J Biol Chem* **280**: 35704–35712.

Comprehensive and Accurate Control of Thermosensitivity of Poly(2-alkyl-2-oxazoline)s via Well-Defined Gradient or Random Copolymerization

Joon-Sik Park[†] and Kazunori Kataoka*[,†,‡,§]

Department of Materials Engineering, Graduate School of Engineering, The University of Tokyo, 7-3-1 Hongo, Bunkyo-ku, Tokyo 113-8656, Japan, Center for Disease Biology and Integrative Medicine, Graduate School of Medicine, The University of Tokyo, Tokyo 113-0033, Japan, and Center for NanoBio Integration, The University of Tokyo, 7-3-1 Hongo, Bunkyo-ku, Tokyo 113-8656, Japan

Received January 16, 2007; Revised Manuscript Received March 10, 2007

ABSTRACT: The lower critical solution temperature (LCST) of the poly(2-alkyl-2-oxazoline)s (POx) was precisely tuned over a broad range of temperatures via the well-defined gradient or random copolymerization between 2-*n*-propyl-2-oxazoline (*n*PrOx) and either 2-isopropyl-2-oxazoline (*i*PrOx) or 2-ethyl-2-oxazoline (EtOx). All the copolymerizations were cationically initiated by methyl *p*-tosylate at the optimum condition (42 °C in acetonitrile) for the living polymerization, resulting in an extremely narrow molecular weight distribution ($M_w/M_n \leq 1.05$). It was determined from the composition analysis by ^{1}H NMR and MALDI−TOF mass spectrometry that the respective monomer reactivity ratios were found to be 3.15 and 0.57 for *n*PrOx and *i*PrOx, respectively, sufficiently different to form the gradient copolymers P(*n*PrOx-*grad*-*i*PrOx), and 1.28 and 1.04 for *n*PrOx and EtOx, respectively, indicating the favorable formation of the random copolymers P(*n*PrOx-*ran*-EtOx). Both gradient and random copolymers followed a simple and practical rule during their LCST modulation, depending on the compositional variation between the hydrophilic/hydrophobic 2-alkyl-2-oxazoline monomers centering on the *i*PrOx. In particular, it was found that poly(2-*n*-propyl-2-oxazoline) (P*n*PrOx) independently exhibited a sharp LCST behavior near room temperature, even comparable to that of poly(2-isopropyl-2-oxazoline) (P*i*PrOx). Furthermore, the P(*n*PrOx-*ran*-EtOx) copolymers were not only synthesized much faster than the gradient copolymers with the *i*PrOx component but also showed a clear phase transition behavior over the wide temperature range from 23.8 to 75.1 °C, offering the most ideal choice, viz., a simple random distribution of the two monomers for tuning the LCST.

Introduction

A great deal of attention has focused on the so-called "smart" polymeric materials showing a discrete change in their propensity that respond to external physical and chemical stimuli, including light, temperature, pH, and magnetic and electric fields. In particular, temperature-responsive polymers are considered useful for various practical applications, such as supports for catalysts,[1] sensors,[2] separation systems,[3] enzymatic bioconjugates,[4] and drug carriers.[5] Drastic changes in the solubility, turbidity, and other physicochemical properties of thermosensitive polymers can be simply induced by adding or removing heat energy, and such feasibility is especially important when designing "smart" polymeric materials that respond to the external stimuli. At this time, careful engineering of the polymer structure should be inevitable in order to realize the precise modulation of the responding temperature as well as the transition sharpness.

In this regard, we have recently established the controlled synthetic route of novel end-functionalized thermosensitive poly(2-isopropyl-2-oxazoline) (P*i*PrOx) telechelics at the optimum condition (42 °C in acetonitrile).[6] The notable LCST-type transition behaviors of P*i*PrOx, characterized by a fast responsivity comparable to the conventional poly(*N*-isopropylacrylamide) (PNiPAAm),[7] could be achieved by the precise control of the well-defined polymeric structures with appreciably narrow molecular weight distributions (MWD) through the living polymerization mechanism. For the development of a thermosensitive drug carrier, P*i*PrOx-based polyion complex (PIC) micelles were also prepared via the complexation of a pair of oppositely charged block ionomers.[8] The PIC micelles exhibited a sharp and constant LCST of 32 °C regardless of the total concentration, demonstrating that the precise control of the polymer structure, such as the molecular weight, MWD, and end group was closely related to the characteristic phase transition behavior of the hierarchal self-assembly like polymeric micelles. Furthermore, the LCST of P*i*PrOx was able to be finely tuned by incorporating the specific composition of the hydrophilic 2-ethyl-2-oxazoline monomer units within the main chains, mainly considering the biorelated application with a LCST near the physiological conditions.[9] In that system, the oxazoline monomers of 2-isopropyl-2-oxazoline and 2-ethyl-2-oxazoline had sufficiently different reactivity ratios of 1.78 and 0.79, respectively, thus offering a useful route to engineer thermosensitive gradient copolymers with an extremely narrow MWD ($M_w/M_n \leq 1.02$).

For now, it is well-known that the length of the alkyl substituents of the poly(2-alkyl-2-oxazoline)s (POx) determines to a large extent their relative hydrophilicity, and only a few 2-alkyl-2-oxazolines (Ox), such as the 2-methyl-, 2-ethyl-, and 2-isopropyl-2-oxazolines, lead to the good solubility of their respective polymers in water at room temperature.[10] Curiously, in the case of the poly(2-ethyl-2-oxazoline) (PEtOx) high polymers with molecular weights above ~20 000, their LCST

* Corresponding author. Telephone: +81-3-5841-7138. Fax: +81-3-5841-7139. E-mail: kataoka@bmw.t.u-tokyo.ac.jp.
† Department of Materials Engineering, Graduate School of Engineering, The University of Tokyo.
‡ Center for Disease Biology and Integrative Medicine, Graduate School of Medicine, The University of Tokyo.
§ Center for NanoBio Integration, The University of Tokyo.

10.1021/ma0701181 CCC: $37.00
Published on Web 04/20/2007

Scheme 1. Synthetic Schemes for the Gradient Copolymerization of *n*PrOx and *i*PrOx and the Random Copolymerization of *n*PrOx and EtOx

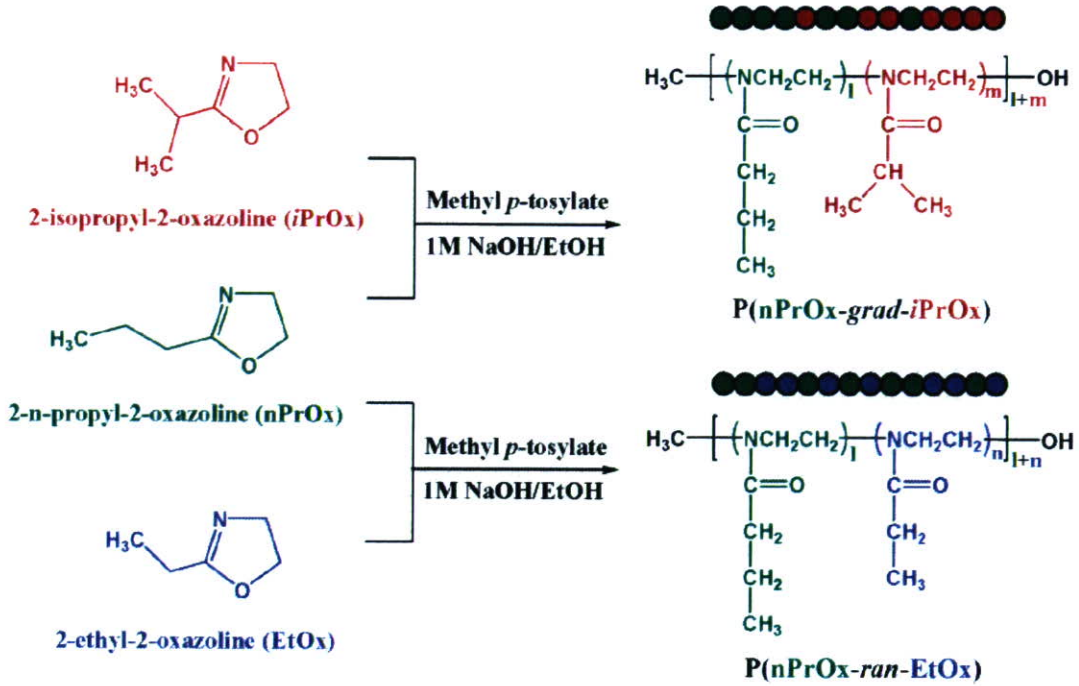

values were observed around 62−65 °C depending on molecular weight and concentration, much higher than that of P*i*PrOx.[11] In this respect, we also focused on the poly(2-*n*-propyl-2-oxazoline) (P*n*PrOx) which has one more hydrophobic methylene group in the side 2-position compared to PEtOx as well as becomes a chemical isomer of P*i*PrOx. Although there is an example investigating the property of the P*n*PrOx-based lipogel (organogel) swollen in organic solvents,[12] the solution properties of the P*n*PrOx oligomers have not yet been studied, especially in terms of their temperature-induced phase transition behavior in water. Moreover, little attention has been paid to the LCST control of POx copolymers except for our recent gradient system, though there are various hydrophobic and hydrophilic Ox monomers such as *n*PrOx, *i*PrOx, and EtOx. Thus, it was highly motivating that a variety of combinations between two Ox monomers with different or similar reactivity ratios could selectively produce the thermosensitive gradient or random POx copolymers according to particular applications.

In this study, we have accomplished the accurate control of the LCST in the POx system over a wide range of temperature by obtaining the well-defined gradient or random copolymers via the selective combination between *n*PrOx and either *i*PrOx or EtOx (Scheme 1). Of special interest is the P*n*PrOx homopolymer independently exhibiting a sharp LCST-type phase transition behavior around 23.8 °C, even comparable to that of P*i*PrOx. To the best of the author's knowledge, this is the first example proving that P*n*PrOx was also soluble in an aqueous solution as well as having a clear thermosensitivity near room temperature. Furthermore, the copolymers composed of *n*PrOx and EtOx resulted in a fully random composition, and also showed a rapid and modulated response to the temperature change from 23.8 to 75.1 °C, considered the most ideal system for tuning the LCST.

Experimental Section

Materials. 2-Isopropyl-2-oxazoline (*i*PrOx) was synthesized from isobutyric acid (Wako Pure Chemical Industries, Ltd., Osaka, Japan) and 2-aminoethanol (Wako Pure Chemical Industries) as previously described.[6] Methyl *p*-tosylate (MeOTs) (Tokyo Kasei Kogyo Co., Ltd., Tokyo, Japan) was distilled from calcium hydride under reduced pressure. 2-Ethyl-2-oxazoline (EtOx) (Aldrich Chemical Co., Ltd., Milwaukee, WI), 2-*n*-propyl-2-oxazoline (*n*PrOx) (Aldrich Chemical Co., Ltd.), and acetonitrile (Wako Pure Chemical Industries) were distilled from calcium hydride following conventional procedures.[13] All other chemicals were used without further purification.

Techniques. The ^{1}H NMR spectra were recorded using a JEOL EX 300 spectrometer at 300 MHz. The chemical shifts were reported in parts per million (ppm) downfield from tetramethylsilane. The molecular weights and molecular weight distributions were determined using a GPC (TOSOH HLC-8220) system equipped with two TSK gel columns ($G4000H_{HR}$ & $G3000H_{HR}$ and SuperAW4000 & SuperAW3000) and an internal refractive index (RI) detector. The columns were eluted with DMF containing lithium bromide (10 mM) and triethylamine (30 mM) at the flow rate of 0.8 mL/min and were maintained at a temperature of 40 °C. The molecular weights (MW) were calibrated using poly(2-isopropyl-2-oxazoline) (P*i*PrOx) standards of which the absolute molecular weights were determined by MALDI−TOF mass spectrometry (Me−P*i*PrOx−OH; MW_{TOF-MS} = 5400, 8700, 11500, 17000). The mass measurements were performed using a MALDI−TOF mass spectrometer (Bruker REFLEX III) operating at an acceleration voltage of 23 kV in the reflection mode. The UV−vis spectra were obtained using a V-550 UV/vis JASCO spectrophotometer.

Synthesis of Homopolymers. The synthetic results of poly(2-isopropyl-2-oxazoline) (P*i*PrOx) and poly(2-ethyl-2-oxazoline) (PEtOx) homopolymers having hydroxyl groups at the ω-terminal ends were taken from our recent account unless otherwise stated.[9]

Poly(2-*n*-propyl-2-oxazoline) (P*n*PrOx) Having a Hydroxyl Group at the ω-Terminal End. 2-*n*-Propyl-2-oxazoline (*n*PrOx) (5.0 g, 44.2 mmol) was added via syringe to a solution of methyl *p*-tosylate (MeOTs) (0.093 g, 0.50 mmol) in acetonitrile (15 mL). The polymerization mixture was stirred at 42 °C for 162.3 h under an argon atmosphere. The mixture was then cooled to room temperature, then treated with methanolic NaOH (1 M) to introduce a hydroxyl group at one of the chain ends (Me−P*n*PrOx−OH).

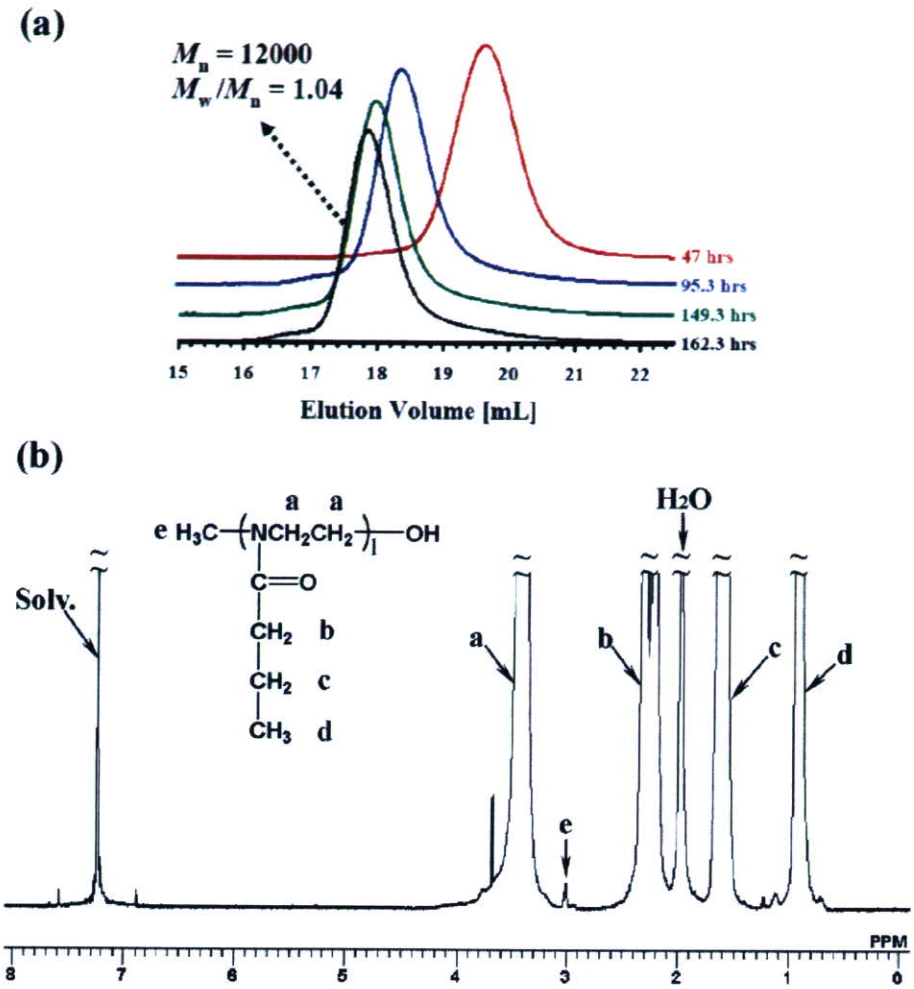

Figure 1. (a) GPC traces of ω-hydroxyl terminated P*n*PrOx homopolymers (Me−P*n*PrOx−OH) with different molecular weights (column, G4000H_{HR} and G3000H_{HR}; P*i*PrOx standard; eluent, DMF (containing 10 mM LiCl and 30 mM TEA); temperature, 40 °C; RI detection) and (b) ^{1}H NMR spectrum of Me−P*n*PrOx−OH in $CDCl_3$ at 25 °C.

Table 1. Gradient Copolymerization Results between *n*PrOx and *i*PrOx at Different Feed Compositions[a] and Their T_{cp} Values

feed ratio (*n*PrOx:*i*PrOx)	yield (%)	M_n (M_w/M_n) MALDI−TOF MS[b]	M_n (M_w/M_n) GPC[c]	*l*:*m*[d]	T_{cp}[e] (°C)
100:0	94	10800 (1.04)	12000 (1.04)	100:0	23.8
75:25	80	11100 (1.01)	13300 (1.03)	80:20	26.3
50:50	88	11400 (1.01)	12300 (1.02)	54:46	30.1
25:75	84	10100 (1.01)	12300 (1.02)	33:67	33.8
0:100	90	10200 (1.01)	9700 (1.02)	0:100	38.7

[a] Reaction conditions: ([*n*PrOx] + [*i*PrOx])/$[MeOTs]_{init.}$ = 88.4, $[MeOTs]_{init.}/[CH_3CN]_{solv.}$ = 0.031 mol/L, 42 °C, terminated with methanolic NaOH (1 M) for hydroxyl ω-end group. [b] Bruker REFLEX III, operating at an acceleration voltage of 23 kV in the reflection mode. [c] DMF (10 mM LiCl and 30 mM TEA), 40 °C, RI detection. [d] Determined by ^{1}H NMR spectroscopy for the final (co)polymer products (monomer composition: *l* = [*n*PrOx], *m* = [*i*PrOx]). [e] Measured by UV−vis spectroscopy (*c* = 1.0 wt %).

The solution of Me−P*n*PrOx−OH was purified via dialysis for 2 days against distilled water and then recovered by lyophilization. Several samples were collected during the course of the polymerization and subjected to the same treatment. The conversion yield and structure of the polymers were analyzed by GPC and ^{1}H NMR spectroscopy (total yields: 4.7 g, 94%).

Synthesis of Gradient Copolymers (P*n*PrOx$_{25\%}$*i*PrOx$_{75\%}$, P*n*PrOx$_{50\%}$*i*PrOx$_{50\%}$, P*n*PrOx$_{75\%}$*i*PrOx$_{25\%}$) Having a Hydroxyl Group at the ω-Terminal End. The respective mixtures of 2-*n*-propyl-2-oxazoline (*n*PrOx$_{25\%}$ = 0.625 g, 5.53 mmol; *n*PrOx$_{50\%}$ = 1.25 g, 11.1 mmol; *n*PrOx$_{75\%}$ = 1.88 g, 16.6 mmol) and 2-isopropyl-2-oxazoline (*i*PrOx$_{75\%}$ = 1.88 g, 16.6 mmol; *i*PrOx$_{50\%}$ = 1.25 g, 11.1 mmol; *i*PrOx$_{25\%}$ = 0.625 g, 5.53 mmol) were added to a solution of MeOTs (0.0465 g, 0.250 mmol) in acetonitrile (8 mL). The polymerization mixture was stirred at 42 °C for 378 h (P*n*PrOx$_{25\%}$*i*PrOx$_{75\%}$), 308.5 h (P*n*PrOx$_{50\%}$*i*PrOx$_{50\%}$), and 206.8 h (P*n*PrOx$_{75\%}$*i*PrOx$_{25\%}$) under an argon atmosphere, respectively. The

Table 2. Random Copolymerization Results between *n*PrOx and EtOx at Different Feed Compositions[a] and Their T_{cp} Values

feed ratio (*n*PrOx:EtOx)	yield (%)	M_n (M_w/M_n) MALDI−TOF MS[b]	M_n (M_w/M_n) GPC[c]	*l*:*n*[d]	T_{cp}[e] (°C)
100:0	94	10800 (1.04)	12000 (1.04)	100:0	23.8
75:25	95	11000 (1.01)	12900 (1.02)	74:26	36.3
50:50	90	10000 (1.01)	12400 (1.02)	53:47	41.8
25:75	88	14000 (1.01)	14000 (1.05)	32:68	50.6
5:95	91	10100 (1.01)	10200 (1.04)	9:91	75.1
0:100	95	8300 (1.01)	8000 (1.02)	0:100	

[a] Reaction conditions: ([*n*PrOx] + [EtOx])/$[MeOTs]_{init.}$ = 88.4, $[MeOTs]_{init.}/[CH_3CN]_{solv.}$ = 0.031 mol/L, 42 °C, terminated with methanolic NaOH (1 M) for hydroxyl ω-end group. [b] Bruker REFLEX III, operating at an acceleration voltage of 23 kV in the reflection mode. [c] DMF (10 mM LiCl and 30 mM TEA), 40 °C, RI detection. [d] Determined by ^{1}H NMR spectroscopy for the final (co)polymer products (monomer composition: *l* = [*n*PrOx], *n* = [EtOx]). [e] Measured by UV−vis spectroscopy (*c* = 1.0 wt %).

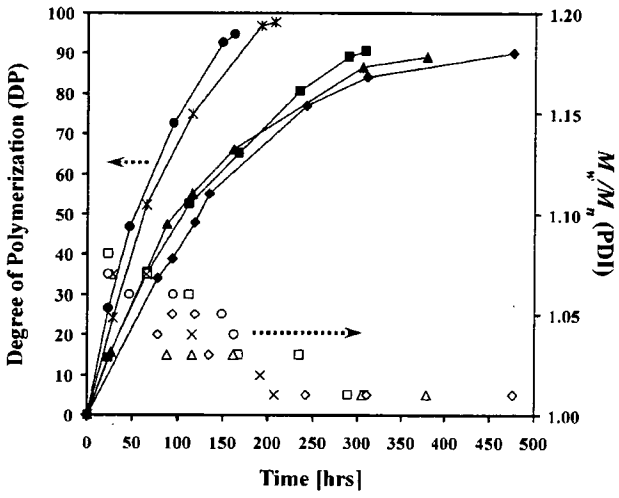

Figure 2. Degree of polymerization (DP) (left ordinate, symbols with dashed lines) and polydispersity index (PDI) (right ordinate), obtained from MALDI–TOF mass spectrometry, vs reaction time for two homopolymers (P*n*PrOx (●, ○), P*i*PrOx (◆, ◇)) and three gradient copolymers (P*n*PrOx$_{25\%}$*i*PrOx$_{75\%}$ (▲, △), P*n*PrOx$_{50\%}$*i*PrOx$_{50\%}$ (■, □), and P*n*PrOx$_{75\%}$*i*PrOx$_{25\%}$ (∗, ×)).

reaction mixtures were cooled to room temperature, and then treated with methanolic NaOH (1 M) to introduce a hydroxyl group at one of the chain ends. The copolymer solutions were purified via dialysis for 2 days against distilled water and then recovered by lyophilization. Several samples of the respective copolymers were collected during the course of the copolymerization. They were subjected to the same treatment as described above, and analyzed by GPC, MALDI–TOF mass, and ^{1}H NMR spectrometers in order to determine the conversion yield and composition of the copolymers (total yields: 2.1 g, 84% (P*n*PrOx$_{25\%}$*i*PrOx$_{75\%}$); 2.2 g, 88% (P*n*PrOx$_{50\%}$*i*PrOx$_{50\%}$); 2.0 g, 80% (P*n*PrOx$_{75\%}$*i*PrOx$_{25\%}$)).

Synthesis of Random Copolymers (P*n*PrOx$_{5\%}$EtOx$_{95\%}$, P*n*PrOx$_{25\%}$EtOx$_{75\%}$, P*n*PrOx$_{50\%}$EtOx$_{50\%}$, P*n*PrOx$_{75\%}$EtOx$_{25\%}$) Having a Hydroxyl Group at the ω-Terminal End. The respective mixtures of 2-*n*-propyl-2-oxazoline (*n*PrOx$_{5\%}$ = 0.126 g, 1.11 mmol; *n*PrOx$_{25\%}$ = 0.626 g, 5.53 mmol; *n*PrOx$_{50\%}$ = 1.250 g, 11.1 mmol; *n*PrOx$_{75\%}$ = 1.873 g, 16.6 mmol) and 2-ethyl-2-oxazoline (EtOx$_{95\%}$ = 2.081 g, 21.0 mmol; EtOx$_{75\%}$ = 1.642 g, 16.6 mmol; EtOx$_{50\%}$ = 1.095 g, 11.1 mmol; EtOx$_{25\%}$ = 0.548 g, 5.53 mmol) were added to a solution of MeOTs (0.0465 g, 0.250 mmol) in acetonitrile (8 mL). The polymerization mixture was stirred at 42 °C for 264.5 h (P*n*PrOx$_{5\%}$EtOx$_{95\%}$), 200 h (P*n*PrOx$_{25\%}$EtOx$_{75\%}$), 235.5 h (P*n*PrOx$_{50\%}$EtOx$_{50\%}$), and 200 h (P*n*PrOx$_{75\%}$EtOx$_{25\%}$) under an argon atmosphere, respectively. The reaction mixtures were cooled to room temperature, and then treated with methanolic NaOH (1 M) to introduce a hydroxyl group at one of the chain ends. The copolymer solutions were purified via dialysis for 2 days against distilled water and then recovered by lyophilization. Several samples of the respective copolymers were collected during the course of the copolymerization. They were subjected to the same treatment as described above, and analyzed using MALDI–TOF mass and ^{1}H NMR spectrometers in order to determine the conversion yield and composition of the copolymers (total yields: 2.0 g, 91% (P*n*PrOx$_{5\%}$EtOx$_{95\%}$); 2.0 g, 88% (P*n*PrOx$_{25\%}$EtOx$_{75\%}$); 2.1 g, 90% (P*n*PrOx$_{50\%}$EtOx$_{50\%}$); 2.3 g, 95% (P*n*PrOx$_{75\%}$EtOx$_{25\%}$)).

MALDI–TOF Mass Spectrometry. An external calibration was performed using poly(2-isopropyl-2-oxazoline) standards (Me–P*i*PrOx–OH; MW = 5400, 8700, 11500, 17000). Ions were generated by laser desorption at 337 nm (N_2 laser, 3 ns pulse width, 10^6–10^7 W/cm^2). For each spectrum, approximately 400 transients were accumulated and all spectra were recorded in the reflection mode. The data evaluation was performed with the Bruker XMASS program using the reflection spectra only in order to achieve a better signal-to-noise ratio. α-Cyano-4-hydroxycinnamic acid (CCA) (Fluka) was selected as a suitable matrix. A trifluoroacetic acid/acetonitrile (0.1% TFA:CH_3CN = 2:1) solution of CCA (10 mg/mL) was mixed with a solution of the polymer in acetonitrile (1 mg/mL) at an equimolar ratio. The resulting mixture was shaken for a few seconds. An aliquot of the mixture (1 μL) was placed on the target plate and inserted into the ion source chamber after being slowly dried. The polymer concentration of the polymer/matrix mixture solution could be diluted for the optimum ionization with an acetone solution of CCA (10 mg/mL).

Turbidity Measurements. Cloud points were determined by spectrophotometric detection of the changes in transmittance (λ = 500 nm) of the aqueous polymer solutions (1.0 wt %) heated at a constant rate (0.5 °C/min). The samples were placed in a temperature-controlled circulating water bath. The cloud point values of the polymer solutions were determined as the temperature corresponding to a 10% decrease in the optical transmittance.

Results and Discussion

Synthesis of Poly(2-*n*-propyl-2-oxazoline) (P*n*PrOx). Prior to the synthesis of a series of gradient and random copolymers, the kinetic behavior of the P*n*PrOx homopolymer was compared with those of P*i*PrOx and PEtOx under identical reaction conditions. To avoid the spontaneously occurring side reactions, such as chain transfer and coupling,[14] all the polymerizations of the respective Ox monomers (*n*PrOx, *i*PrOx, and EtOx) were conducted under mild temperature conditions (42 °C in acetonitrile).

The cationic ring-opening polymerization of *n*PrOx, initiated with MeOTs in acetonitrile, was done to obtain the poly(2-*n*-propyl-2-oxazoline) carrying a hydroxyl group at the ω-end (Me–P*n*PrOx–OH) under a mild temperature condition (42 °C). After the polymerization was left to proceed for ca. 162.3 h, it was ascertained from the GPC diagrams (Figure 1a) that the time-dependent change in the number-average molecular weight (M_n) and the molecular weight distribution were almost consistent with the living polymerization process; for the final product, the polydispersity index was low (PDI $_{GPC}$ = 1.04, PDI$_{TOF-MS}$ = 1.04) and the experimental M_n value ($M_{n,GPC}$ = 12 000, $M_{n,TOF-MS}$ = 10 800) was close to the value predicted from the initial monomer/initiator ratio [$M_{n,calcd}$ = 10 000] (Tables 1 and 2). The ^{1}H NMR spectrum of Me–P*n*PrOx–OH in $CDCl_3$ (Figure 1b) presented a broad singlet at δ 3.39 ppm attributed to the resonance of the methylene protons on the polymer backbone, a broad singlet at δ 0.90 ppm ascribed to the resonance of the methyl protons of the *n*-propyl group on the polymer side chain, and a singlet at δ 3.01 ppm due to the resonance of the α-terminal methyl protons. However, in the case of the P*n*PrOx polymerization, the side reactions, such as chain transfer and coupling, were slightly more pronounced than the other POx systems, such as P*i*PrOx and PEtOx, as seen from the GPC charts with a lower molecular weight tailing and a higher molecular weight shoulder. It was likely that the pK_a values of the methine (CH) at the 2-isopropyl group of *i*PrOx and the methylene (CH_2) at the 2-*n*-propyl group of *n*PrOx and the 2-ethyl group of EtOx in proximity to the cationic oxazolinum ring were related to the difficulty level of proton abstraction by the *p*-tosylate anion. This assumption could be supported by applying Hammett's substituent constant (σ) values taken from a conventional reference.[15] It was thus calculated to be σ_{iPr} = −0.340 for CH at the 2-isopropyl group with two CH_3, σ_{nPr} = −0.144 for CH_2 at the 2-*n*-propyl group with one C_2H_5 and one H, σ_{Et} = −0.170, for CH_2 at the 2-ethyl group with one CH_3 and one H. To put it more concretely, the substituent effect, viz., abundance of electron density on the carbon (C) of the methine (CH) and methylene (CH_2) of the respective 2-alkyl groups could be expressed in the order 2-*n*-propyl < 2-ethyl ≪ 2-isopropyl, indicating that the methylene proton of the 2-*n*-

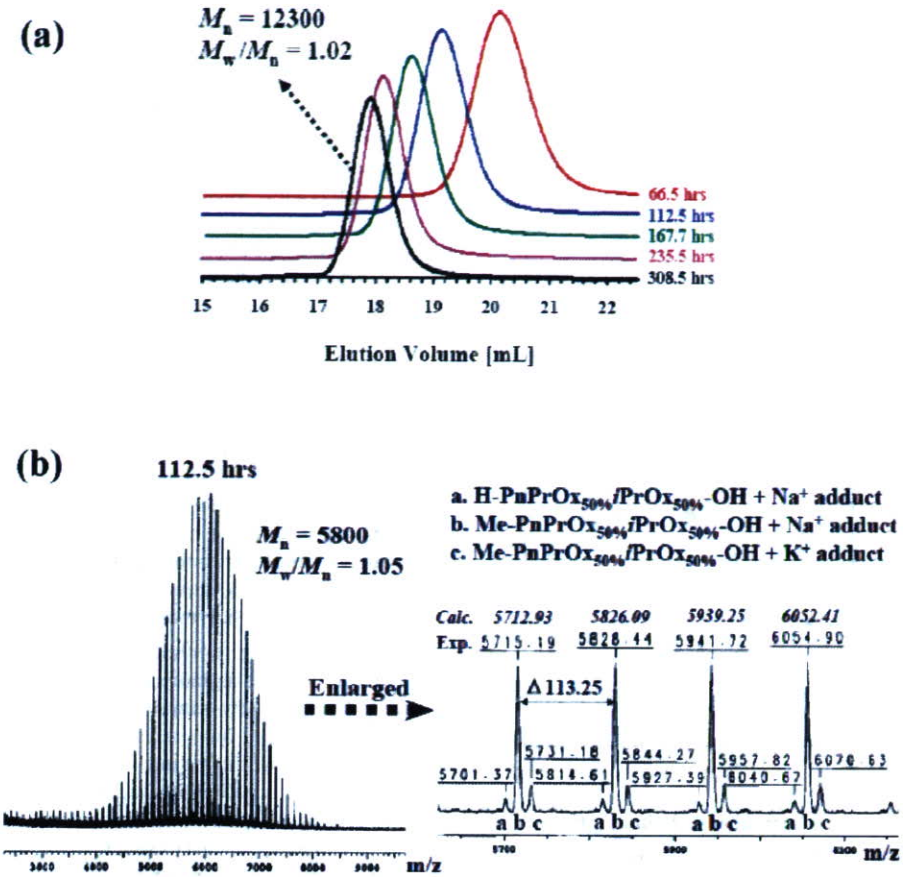

Figure 3. (a) GPC trace of P*n*PrOx$_{50\%}$*i*PrOx$_{50\%}$ copolymer samples with different molecular weights (column, G4000H$_{HR}$ and G3000H$_{HR}$; P*i*PrOx standard; eluent, DMF (containing 10 mM LiCl and 30 mM TEA); temperature, 40 °C; RI detection) and (b) MALDI−TOF mass spectrum of P*n*PrOx$_{50\%}$*i*PrOx$_{50\%}$ after 112.5 h (left) and its expanded spectrum in the mass region of 5700−6100 (right).

propyl group was most likely to be withdrawn under the same reaction conditions.

The time-dependent monomer conversion into the backbone for the respective homopolymers of *n*PrOx, *i*PrOx, and EtOx were obtained from the MALDI−TOF mass spectrometry as depicted in Figures 2 and 6, whereby the degree of polymerization (DP) was positioned on the left ordinate and the polydispersity index (PDI) (M_w/M_n) on the right ordinate. From the time-dependent DP and PDI changes of the respective homopolymers, it was obvious that the polymerization rates of both *n*PrOx and EtOx were much faster than that of *i*PrOx as well as *n*PrOx was slightly faster than EtOx. As far as the slower polymerization rate of *i*PrOx was concerned, it was reasonable to suppose that the bulky structure of the 2-isopropyl group could be sterically unfavorable for the rapid propagation.

Synthesis of Gradient Copolymers. In view of the synthetic result of the homopolymers described above, we synthesized a series of copolymers comprising *n*PrOx and *i*PrOx in order to explore the hydrophobic contribution of *n*PrOx on the LCST of the P(*n*PrOx-*grad*-*i*PrOx) copolymers (Scheme 1). The respective mixtures of 2-*n*-propyl-2-oxazoline (*n*PrOx$_{25\%}$, 5.53 mmol; *n*PrOx$_{50\%}$, 11.1 mmol; *n*PrOx$_{75\%}$, 16.6 mmol) and 2-isopropyl-2-oxazoline (*i*PrOx$_{75\%}$, 16.6 mmol; *i*PrOx$_{50\%}$, 11.1 mmol; *i*PrOx$_{25\%}$, 5.53 mmol) were added to a solution of MeOTs (0.250 mmol) in acetonitrile and polymerized at 42 °C, as in the case of the two homopolymers (P*n*PrOx and P*i*PrOx). The synthesis results of three copolymers (P*n*PrOx$_{25\%}$*i*PrOx$_{75\%}$, P*n*PrOx$_{50\%}$*i*PrOx$_{50\%}$, and P*n*PrOx$_{75\%}$*i*PrOx$_{25\%}$) with the same initial monomer/initiator ratio (DP$_{calcd}$ = 88.4) are summarized in Table 1. The polymerization behaviors of the copolymers with the initial *n*PrOx and *i*PrOx molar ratios of 25%:75%, 50%:50%, and 75%:25% were characterized by the time-dependent

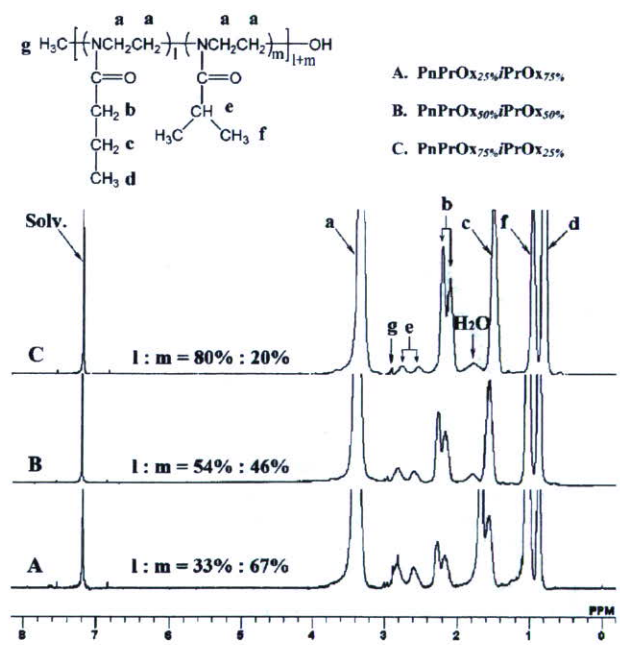

Figure 4. ^{1}H NMR spectra for the final products of three gradient copolymers (P*n*PrOx$_{25\%}$*i*PrOx$_{75\%}$, P*n*PrOx$_{50\%}$*i*PrOx$_{50\%}$, and P*n*PrOx$_{75\%}$*i*PrOx$_{25\%}$) in $CDCl_3$ at 25 °C.

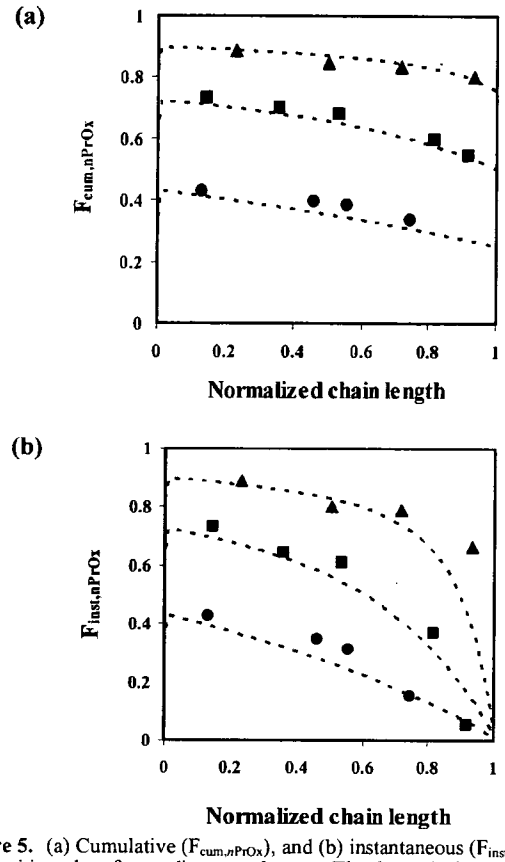

Figure 5. (a) Cumulative ($F_{cum,nPrOx}$), and (b) instantaneous ($F_{inst,nPrOx}$) composition plots for gradient copolymers. The theoretical prediction curves (dotted) were calculated using the simulation program PROCOP[17] (P*n*PrOx$_{25\%}$*i*PrOx$_{75\%}$ (●), P*n*PrOx$_{50\%}$*i*PrOx$_{50\%}$ (■), and P*n*PrOx$_{75\%}$*i*PrOx$_{25\%}$ (▲)).

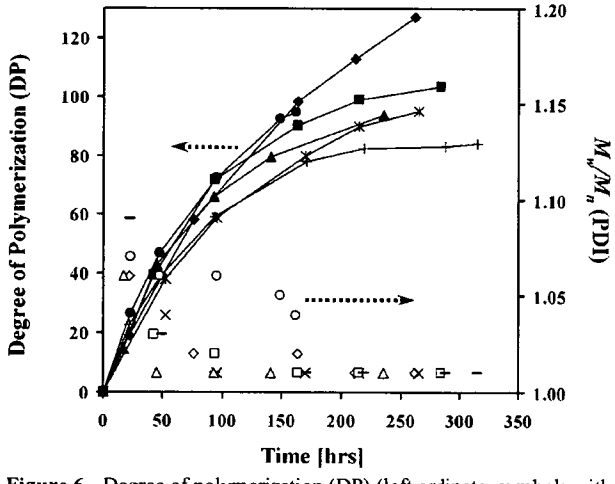

Figure 6. Degree of polymerization (DP) (left ordinate, symbols with dashed lines) and polydispersity index (PDI) (right ordinate), obtained from MALDI–TOF mass spectrometry, vs reaction time for two homopolymers (P*n*PrOx (●, ○), PEtOx (+, −)) and four random copolymers (P*n*PrOx$_{5\%}$EtOx$_{95\%}$ (*, ×), P*n*PrOx$_{25\%}$EtOx$_{75\%}$ (♦, ◇), P*n*PrOx$_{50\%}$EtOx$_{50\%}$ (▲, △), and P*n*PrOx$_{75\%}$EtOx$_{25\%}$ (■, □)).

change in the DP and PDI via the MALDI–TOF mass and GPC traces, as seen in Figures 2 and 3. Regardless of the comonomer ratio in the feed, the experimental degree of polymerization (DP from MALDI–TOF mass spectrometry) of the respective copolymers was close to the predicted value from the initial monomer/initiator ratio (DP_{calcd} = 88.4) and their molecular weight distributions were quite narrow in all cases (Figure 2).

The GPC trace of P*n*PrOx$_{50\%}$*i*PrOx$_{50\%}$, which was sampled at different polymerization times, also showed an increase in the molar mass with time and symmetrical monomodal peaks, as shown in Figure 3a. Similar results for the other two copolymers (P*n*PrOx$_{25\%}$*i*PrOx$_{75\%}$ and P*n*PrOx$_{75\%}$*i*PrOx$_{25\%}$) with different monomer ratios in the feed were also confirmed by the respective GPC traces (data not shown). Although the detailed analysis of the copolymer composition and sequence distribution for P*n*PrOx$_{50\%}$*i*PrOx$_{50\%}$ could not be done due to the same mass value between *n*PrOx and *i*PrOx ($M_{n,nPrOx} = M_{n,iPrOx}$), the end group analysis was conducted using the MALDI–TOF mass spectrum recorded after 112.5 h (Figure 3b). The most and second intense signals were assigned to the sodium and potassium adducts of Me–P*n*PrOx$_{50\%}$*i*PrOx$_{50\%}$–OH with α-methyl and ω-hydroxyl terminal groups, respectively, while the third intense signal was due to the sodium adduct of H–P*n*PrOx$_{50\%}$*i*PrOx$_{50\%}$–OH as a result of the undesirable proton initiation. In addition, the compositions of the final copolymer products determined by ^{1}H NMR spectrometry were almost in good agreement with the calculated values from the feed ratio of both monomers, indicating their quantitative conversion into the respective copolymers (Figure 4 and Table 1).

In this living polymerization system, copolymers were expected to have a gradient composition, providing sufficiently different reactivity ratios of the two monomers, *n*PrOx and *i*PrOx. Indeed, from the compositional analysis by ^{1}H NMR spectrometry of the respective copolymer samplings (monomer conversions: ca. 20–40%) plotted in Figure 2, the reactivity ratios of the respective monomers were calculated to be r_{nPrOx} = 3.15 and r_{iPrOx} = 0.57 using the nonlinear Tidwell–Mortimer (TM) method,[16] showing the most reasonable result for the additional composition analysis of the copolymers. Determination of the reactivity ratio at a low conversion could be affected by the different reactivity of the initiator against a specific monomer, therefore, we selected monomer conversions of ca. 20–40% as a reasonable interval in this living system of which the high polymer was not immediately formed by the reaction.[17] This difference in the reactivity ratios of the two monomers indicates that *n*PrOx should initially be consumed much faster than *i*PrOx. However, because of the decreasing concentration of the former in the residual feed, the rate of its incorporation into the polymer chain also decreased. This resulted in an increased instantaneous incorporation of *i*PrOx into the copolymer as the reaction progressed and ultimately in the formation of an *i*PrOx-rich chain end. Because of the simultaneous initiation and uniform propagation kinetics in this living system as known from the appreciably low polydispersity indices, each polymer chain should display a similar trend of a gradually decreasing *n*PrOx and an increasing *i*PrOx composition along the backbone from the α-terminal to the active ω-chain end. The cumulative and instantaneous composition plots ($F_{cum,nPrOx}$ and $F_{inst,nPrOx}$, respectively) vs the normalized chain length were obtained for the three copolymerizations with different initial molar ratios of *n*PrOx and *i*PrOx in the feed (Figure 5). According to the experimental plots, the shape of the obtained gradient copolymers closely followed the theoretical predictions using r_{nPrOx} = 3.15 and r_{iPrOx} = 0.57.[18] This type of methodology was useful to trace the composition drift of the gradient copolymers, as in the system of atom transfer radical copolymerization.[17]

Synthesis of Random Copolymers. On the basis of the synthetic result of two *n*PrOx and EtOx homopolymers showing similar polymerization rates, we next synthesized a series of